Power ramped cladding stresses and strains in 3D simulations with burnup-dependent pellet-clad friction

J. Sercombe, I. Aubrun, C. Nonon

Power ramped cladding stresses and strains in 3D simulations with burnup-dependent pellet-clad friction

J. Sercombe[a], I. Aubrun[b], C. Nonon[c]

[a] D. Sc., Res. Eng., CEA, DEN, DEC/SESC, F-13108 Saint-Paul-lez-Durance, France, jerome.sercombe@cea.fr.

[b] D. Sc., Res. Eng.,CEA, DEN, DEC/SA3C, F-13108 Saint-Paul-lez-Durance, France.

[c] PCI Project manager, CEA, DEN, DEC, F-13108 Saint-Paul-lez-Durance, France.

Abstract

This paper presents 2D(r,θ) plane strain and 3D simulations of PCI during base irradiation and ramp tests. Inverse analysis is used to estimate the evolution of friction at the pellet-clad interface with burnup. The number of radial cracks that form during power ramp tests in seventeen UO_2-Zy4 rodlets with burnups in the range 20-60 GWd/tU is the main parameter on which inverse analysis is based. It is shown that the sole evolution of the friction coefficient with burnup is sufficient to capture the radial crack pattern of the rodlets after power ramping. A simple relation between the friction coefficient and the burnup variation after initial pellet-clad contact is thus proposed and used in 3D simulations of PCI. The delayed gap closing at Mid-Pellet level with respect to Inter-Pellet level leads to an axial variation of the friction coefficient, with maximum values near the pellet ends. The consequences in terms of PCI failure propensity are then discussed.

Introduction

Failure of zirconium alloys fuel rods by Pellet Cladding Interaction (PCI) has been studied worldwide for many years (Cox, 1990) but remains a matter of concern since

no absolute remedy has yet been found. On a mechanical standpoint, the main parameters that govern PCI failures are however well known : pellet hourglassing or wheat sheaf due to the high radial thermal gradient in the pellet which leads to over-straining of the cladding in front of pellet ends (Aas, 1972, Levy and Wilkinson, 1974), pellet radial cracking which induces strain-stress concentration in the cladding (Gittus, 1972). In the 70's and 80's, this last mechanism has been studied in details through the development of elastic two-dimensional analytical or numerical models (Gittus, 1972, Jackson, 1987, Nakatsuka, 1981a, Nerman, 1980, Ranjan and Smith, 1980, Roberts, 1978, Yu et al., 1990). From these studies, two main points have been deduced : first, friction at the pellet-clad interface is by far the dominant parameter with respect to stress concentration in the cladding (it maximizes interfacial shear stresses). Second, stress concentration decreases with the number of pellet fragments, i.e., with shear stress relaxation induced by pellet cracking. Recently, non-linear analyses have been performed and led to similar conclusions (Brochard et al., 2001, Marchal et al., 2009, Michel et al., 2008a). Brochard et al. (2001) demonstrated by two-dimensional simulations of the contact between a plastic pellet fragment and a viscoplastic cladding that clad hoop strains and stresses increase to a maximum with the pellet-clad friction coefficient. Michel et al. (2008a) pointed in their three-dimensional simulations the reduction in shear stresses at pellet ends with increasing radial cracking of the pellets.

In some early works on PCI, some discussion obviously took place on what value for the friction coefficient should be considered as representative of real pellet-clad interaction (Smith, 1979). Closed-form solutions concerned this time with the estimation of circumferential stresses at the periphery of a pellet fragment due to interfacial shear loading were derived (Rolstad, 1975, Smith, 1979). They basically showed that the higher the friction coefficient at the pellet-clad interface, the higher the circumferential stress. The calculated maximum stress was then compared to available experimental measures of the tensile strength of the material, ~ 100 MPa (Evans and Davidge, 1969, Radford, 1979). It lead to the conclusion that a typical radial crack pattern with 10 fragments after normal operating conditions in a

commercial reactor would be consistent with a friction coefficient of less than 1. The main outcome of these studies was however the correlation that exist between fuel radial cracking and friction at the pellet-cladding interface. A nice and unique experimental proof of this relation is available in the work of Wood et al. (1980) on graphite-lubricated fuel rods. In laboratory experiments, they measured a reduction in friction by a factor 3 due to graphite lubrification. In systematic Post-Irradiation Examinations (PIE) after ramp tests, they then observed an important reduction of pellet radial cracking in graphite lubricated rods with respect to standard rods.

Friction between pellet and cladding has also been measured experimentally in a number of laboratories (Nakatsuka, 1981b, Shchavelin et al., 1984, Swota et al., 1966, Tachibana et al., 1977, Wood et al., 1980). Test conditions vary in function of fuel oxide type and surface conditions (roughness), cladding type and preparation (autoclaved or not), temperature, sliding speed, geometry of tested specimen (flat or curved), ... A synthesis of the results can be found in Brochard et al. (2001). It basically shows that most of the tests on non-irradiated samples give friction coefficients between 0.4 and 0.7, irrespective of temperature, cladding and oxide surface preparation. A rather different picture has been obtained from in-pile friction tests (Baranov et al., 2007, Bozhko et al., 1991, Shchavelin et al., 1986). A significant increase of the friction coefficient from 0.4 to 1.2 has been observed, depending on the fluence and the thermal neutron flux.

In the last two decades, international efforts have been devoted to the study of fuel at high burnup. A common feature of high burnup fuel rods, irrespective of the reactor, pellet and cladding type, is the strong pellet-clad bonding at the interface that is observed at cold End-Of-Life (EOL) state (Desgranges, 1998, Nogita and Katsumi, 1997, Tanaka, 2006, Van der Berghe et al., 2004, Walker et al., 1997, Yagnik et al., 1999). Generally, bonding is associated with the development of a (U,Zr)O_2 reaction layer (with or without cesium) at the interface between the pellet rim and internal zirconia (Nogita and Katsumi, 1997, Tanaka, 2006). Nogita and Katsumi (1997) attribute the formation of the reaction layer to the phase transformation of zirconia

(from monoclinic to cubic) due to the fission reactions that take place at the pellet periphery when strong pellet-clad contact occurs. This hypothesis is consistent with the previously mentioned in-pile friction tests which showed some evolution of the friction coefficient with irradiation.

Literature review indicate that friction at pellet-clad interface is a crucial parameter with respect to PCI-driven rod failures. It also shows that it evolves with irradiation (burnup). An experimental characterization of friction evolution during irradiation is very difficult to achieve and requires very sophisticated equipments. It can however be correlated to radial cracking of the pellet which can be more easily measured. In this paper, an inverse analysis based on two-dimensional simulations of UO_2 pellet cracking during power ramps is proposed in order to establish a correlation between friction and burnup evolution after initial pellet-clad contact. The calculated radial crack patterns are compared to those estimated from optical ceramographies performed on radial cuts. The proposed relation is then used in three-dimensional simulations of pellet-clad interaction and the consequences of time- and space-dependent friction on PCI failure propensity analyzed.

2. Pellet radial cracking.

2.1. Mechanisms and main trends

The irradiation history during normal (base irradiation) and off-normal (power ramps) operating conditions together with the radial crack pattern of the pellet is schematically described in Figure 1. The mechanisms by which pellet cracking occurs during normal operating conditions have been studied by means of 2D or 3D finite element simulations (Diard, 2001, Levy and Wilkinson, 1974, Oguma, 1983) and may be summarized as follows. During startup, the radial thermal gradient in the pellet give rise to high circumferential and axial tensile stresses at the pellet periphery. In consequence, radial and transverse cracking occurs. Oguma (1983) showed that radial cracking is initiated at a low power level (60 W/cm) and that

the number of fragments increases step-wise with the rod power. At hot state, radial crack propagation towards the pellet center is limited by the compressed central part of the pellet (Levy and Wilkinson, 1974). During cooling down, compressive stresses are progressively relieved and radial cracks might then extend towards the pellet center generally leading to well divided pellet fragments as illustrated in Figure 2 (left) by cross-sections of UO_2 pellets (Nonon et al., 2004). The number of pellet fragments after irradiation depends mainly on the power level reached in reactor. It doubles step-wise with the rod power (Oguma, 1983). For PWR conditions (mean rod power around 200 W/cm), the 3D simulations performed by Diard (2001) led to a stable configuration for a fuel pellet divided in 8 radial fragments. It is important to stress that radial cracking during base irradiation occurs mainly when the pellet-clad gap is open and that it is reasonably described by simulations assuming an elastic behavior for the materials (creep can be neglected).

The situation is rather different during power ramps. First, the pellet-clad gap is closed. The temperature in the pellet is higher and leads to significant creep of the material which is at the origin of dish filling (Sercombe et al., 2009). The strong pellet-clad interaction upon power increase leads furthermore to high stresses in the cladding with possible plastic and viscoplastic flow. The stable crack pattern obtained after the first power cycle in normal operating conditions is modified by power rise and the development of new radial and axial cracks initiated at the pellet periphery can be observed, as illustrated in Figure 2 (middle and right) by cross-sections of UO_2 pellets after ramp tests (Nonon et al., 2004). The radial extension of these secondary cracks is limited by the size of the (visco)plastic central region of the fuel pellet under compression. Power shutdown leads to radial tensile stresses at the boundary between the highly deformed (visco)plastic central part of the pellet and the elastic outer layer and hence to circumferential cracking. Circumferential cracking is particularly important when viscoplastic flow has been consequent, i.e., in ramp tests with important holding times, as illustrated in Figure 2 (right).

2.2. Characterization of UO_2-Zy4 fuel rod cracking.

In this part, fuel radial cracking as measured after power ramps performed for most of them in the Osiris experimental reactor (Mougel et al., 2004) on UO_2 - Stress-Relieved-Annealed Zircaloy 4 (SRA Zy-4) rodlets is analyzed in details to study the impact of power level, holding time and burnup. The main characteristics of the database are summarized in Table 1. The ramp tests cover a wide range of burnup ($25-60$ GWd/tU), maximum power ($400-530$ W/cm) and holding time ($0-12$h). The number of radial cracks after each power ramp has been measured from radial cross-sections of the rodlets. Most of the measurements have been made on radial cross-sections located at Mid-Pellet (MP) level (centered with respect to pellet ends). In some cases, estimates of radial cracking are available on cross-sections situated near the pellet ends and will be referred as Inter-Pellet (IP) in the paper.

A distinction between radial cracks formed during base irradiation (BI cracks) and ramp tests (PR cracks) has been made based on the radial extension of the cracks : base irradiation cracks usually reach the pellet center, power ramp cracks are usually circumscribed by the intragranular bubbles precipitation radius which roughly defines the outer limit where gas swelling and fuel creep takes place. The methodology employed for radial crack counting is illustrated for fuel rodlet F2 in Figure 3. The number of radial cracks after base irradiation (BI cracks) refers to the radial cracks in the cross-section that extend over the intragranular bubbles precipitation radius and reach the pellet center. The others are classified as radial cracks formed during ramp tests (PR cracks). From cross-counting comparisons, the uncertainty in the counting process has been estimated around 10%.

2.3. Evolution of fuel rod cracking with burnup.

The post-ramp crack measurements have been used in Figure 4 to plot the evolution of the number of radial cracks at the end of base irradiation versus the mean burnup of the fuel rodlet. Only the measures made at Mid-Pellet level have been used. Figure 4 shows that there is no visible evolution of radial pellet cracking during

normal operating conditions with burnup. The average number of pellet cracks is close to 10 with a standard deviation of ± 3. This estimate is consistent with the 3D calculations of Diard (2001) where a stable cracked configuration was found with 8 fragments.

The evolution of the number of radial cracks formed during ramp tests versus the mean burnup of the fuel rodlet is plotted in Figure 5. The number of available measures and the dispersion makes any direct conclusion objectionable. There are however a few points that can be discussed. First, all the rodlets irradiated 2 cycles (~ 25 GWd/tU) prior to ramp testing have a similar number of radial cracks ($10 - 15$). This seems relatively independent of the maximum power in the power ramp and of the holding time. Second, there is a clear evolution when radial cracks of rodlets irradiated 4 cycles (burnup ~ 50 GWd/tU) are compared to the former. With an average value close to 50, these high burnup fuel rods are much more fractured during power ramps. The situation for fuel rodlets irradiated 3 cycles (~ 40 GWd/tU) is less clear with a strong variation of the measured number of radial cracks ($15-50$). However, there seem to be a strong impact of the holding time with $15 - 30$ cracks for rodlets ramped at maximum power for less than 15 minutes and $45 - 50$ cracks when the holding time exceeds 1h. The higher contribution of pellet gas-induced swelling to pellet-clad interaction in high burnup fuel rods, particularly during holding time, could be one reason for this specific behavior. From Table 1, it may further be noticed that there is no direct relation between the number of radial cracks and the maximum power reached during the ramp (the 3 cycles rods J3 and K3 ramp tested at a high power ~ 520 W/cm with a short holding time < 15 minutes have less radial cracks that the H3 and I3 rods with a long holding period > 1h and a much smaller power ~ 420 W/cm).

Analyzing the database in terms of a single parameter dependency (burnup) is of course not sufficient to catch all the complexity of pellet-clad interaction. As shown in Figure 5, the holding time seems to be of importance and the data could obviously be split in two different batch. As a matter of fact, pellet clad interaction is modified

by burnup due to several factors which depend on ramp test conditions (power increase, holding time, ...), on pellet behavior (enhanced thermal strains and gas-induced swelling, ...) and on clad behavior (enhanced clad temperature due to corrosion with possible increase of creep and plastic flow, ...). An in-depth analyses of these different factors requires the use of sophisticated fuel codes which incorporate the different phenomena taking place during pellet-clad interaction.

3. Simulation of PCI during power ramps.

3.1. Overview of Alcyone fuel code

Alcyone is a multi-dimensional application (Sercombe et al., 2009) which consists of four different schemes concerned with:

- the complete fuel rod discretized in axial segments (1D),
- half of the pellet and the overlying cladding (2Drz),
- one quarter of a pellet fragment and associated cladding (3D), see Figure 6, where the mid-pellet plane is situated at the top of the mesh,
- the mid-pellet plane of the 3D pellet scheme (2Drθ), see Figure 7.

The different schemes use the Finite Element (FE) code Cast3M (Cast3M, 2011) to solve the thermo-mechanical problem and share the same physical material models at each node or integration points of the FE mesh. This makes the comparison of simulated results from one scheme to another possible with no dependency on the constitutive models. The main phenomena considered in the thermo-mechanical code Alcyone are summarized in Table 2. In connection with the aim of this paper, a more detailed description of the pellet creep and crack models, of the clad creep and plasticity models and of the pellet-clad friction model will be given in the next parts. It must be emphasized that many non-linear behavior are considered simultaneously (creep, cracking, plasticity, friction, stress-dependent gas swelling, ...) in

the simulations which makes it a very interesting tool for studying separate effects. The general performance of Alcyone's schemes has been checked by comparing its results to that obtained from a broad range of base irradiations and ramp tests (more than 200) performed on UO_2-Zy4, UO_2-M5 and MOX-Zy4 fuel rods with a burnup up to 60 GWd/tU. It was found that Alcyone predicts with reasonable accuracy the residual clad diameters, the corrosion thickness, the rod elongations, the fission gas release and internal pressure of the rods after normal and off-normal operating conditions (Sercombe et al., 2009).

Hereafter, the 2D(r,θ) and 3D schemes of Alcyone will be used to simulate pellet cracking during base irradiation and power ramps. The main hypotheses underlying the development of these two schemes can be stated as follows. To be consistent with base irradiation cracking, it is assumed at the beginning of the calculations that the pellet is initially divided in 8 identical fragments. In the 3D scheme, only one quarter of a single pellet fragment and the overlying piece of cladding are meshed (see Figure 6). The pellet description accounts for the geometrical particularities of the fuel element (dishing, chamfer, ...). The 2D(r,θ) scheme describes the behavior of the mid-pellet plane of the fragment, see Figure 7. It is an intermediate configuration which can be used to assess precisely stress concentration in the cladding near a pellet crack tip (Michel et al., 2008a).

The boundary conditions in 3D and 2D(r,θ) are shown in Figure 6 and 7, respectively. They account for the geometrical symmetries of the problem and for the pellet-cladding and pellet-pellet interactions. Pellet-pellet inter-penetration along the fracture plane Ox_0z (line Px_1 in 2D(r,θ)) is forbidden by the unilateral contact condition $U_y \geq 0$. At the inter-pellet plane (plane Ox_0y_0 in Figure 6), unilateral contact conditions are prescribed ($U_z \geq 0$ with U_z the axial displacement). To account for the mechanical reaction of the fissile column above and under the meshed fragment, an axial locking condition between the pellet and the cladding mid-planes is enforced when the pellet-clad gap is closed ($U_z^{pellet} = U_z^{clad}$ on plane Px_1y_1 in 3D, see Figure 6). Generalized plane strain conditions are considered in 2D(r,θ) which

allows to model the out-of-plane stresses and strains. In consequence, the axial locking condition is also enforced, i.e., $\epsilon_z^{pellet} = \epsilon_z^{clad}$.

Concerning loading conditions, the internal pressure (gas pressure) is applied to the cladding inner surface and to the pellet fragment outer surface. The external pressure (water pressure) is applied to the cladding outer surface. The temperature of the cladding surface in contact with the coolant and the pressure of the coolant are extracted from 1D fuel rod simulations and applied directly as boundary conditions in the 2D(r,θ) and 3D calculations. Internal pressure of the fuel rod is however re-calculated at each time step from the width of the pellet-clad gap and by assuming that the contribution of the lower and upper plenum of the fuel rod to the free volume can be equally shared between the pellets. At the pellet-cladding interface, unilateral contact is assessed and a Coulomb model is introduced to simulate friction-slip or adherence.

3.2. Pellet cracking and creep model.

Pellet radial cracking during base irradiation is taken into account through the modeling of a pellet fragment with adequate boundary conditions (fracture plane). In order to account for additional pellet cracking during power ramps and for thermal creep, a continuum approach has been developed and detailed in Michel et al. (2008b). The stress-strain constitutive law for the fuel material is given by Hooke's law as follows :

$$\boldsymbol{\sigma} = \boldsymbol{C} : (\boldsymbol{\epsilon} - \boldsymbol{\epsilon}^{vp} - \sum_{i=1}^{3} \epsilon_i^c \boldsymbol{n}_i) \tag{1}$$

with $\boldsymbol{\sigma}$ the stress tensor, $\boldsymbol{\epsilon}$, the total strain tensor and $\boldsymbol{\epsilon}^{vp}$ the creep strain tensor. ϵ_i^c refer to the crack strain component in direction i with its associated normal tensor $\boldsymbol{n}_i$. $\boldsymbol{C}$ is the fourth-order elastic tensor.

While a non-brittle behavior is assumed in compression (creep only), the yield stress of the material in tension is described by three independent failure criteria :

$$f_i = \sigma_i - R_i(\epsilon_i^c) \leq 0 \tag{2}$$

In eq. 2, σ_i refers to the stress component in direction i, R_i is the fuel residual tensile strength in direction i. Since normal or off-normal operating conditions lead generally to radial, circumferential and axial cracks, the orientation of cracks is assumed constant in time and prescribed by the cylindrical coordinate system ($i = r, \theta, z$). The development of micro-cracking once the yield stress is reached and till complete failure of the material is represented by a linear softening law, as expressed by the following equation :

$$R_i(\epsilon_i^c) = \langle f_i^t - K_i \epsilon_i^c \rangle \tag{3}$$

with f_i^t and K_i respectively as the fuel tensile strength and the softening modulus in direction i. $\langle A \rangle = A$ if $A > 0$ and 0 if $A \leq 0$. The crack strain rate in direction i (r,θ,z) is given by the consistency condition $\dot{f}_i = 0$ in the following form :

$$\dot{\epsilon}_i^c = -\frac{\dot{\sigma}_i}{K_i} \tag{4}$$

The stress-strain relationship obtained from Eqs. 1-4 in any direction ($i = r, \theta, z$) is illustrated in Figure 8 (left) along path 0-1 (elastic loading), path 1-2 (softening part with a decreasing tensile strength R_i) and path 2-3 (fully cracked material with no residual strength $R_i = 0$). Expressions 2-4 are applicable only for monotonic loading conditions during which crack openings tend to increase. During normal operating conditions in reactor, the fuel undergoes loading cycles which can lead to crack reclosing. As illustrated schematically in Figure 8 (right), crack reclosing or/and re-opening are taken into account by modifying the elastic modulus of the material such that $\epsilon_i^c = 0$ when $\sigma_i = 0$ (path 2-0 and 3-0). The history of crack-induced damage is thus described by the residual tensile strength variable R_i.

The constitutive law describing creep of UO_2 involves three Newtonian creep mechanisms with different kinetics: irradiation creep, scattering-creep for small stresses and low temperatures and dislocation-creep for large stresses and high temperatures (Monerie and Gatt, 2006). Creep strain rate is given by the following relation:

$$\dot{\boldsymbol{\epsilon}}^{vp} = \dot{\boldsymbol{\epsilon}}^{irr} + (1 + \alpha\phi) \left[(1 - \theta) \dot{\boldsymbol{\epsilon}}^{scat} + \theta \dot{\boldsymbol{\epsilon}}^{disl} \right] \tag{5}$$

in which $\dot{\boldsymbol{\epsilon}}^{irr}$, $\dot{\boldsymbol{\epsilon}}^{scat}$ and $\dot{\boldsymbol{\epsilon}}^{disl}$ are respectively the irradiation, scattering and dislocation creep strain rate tensors. The latter obey the normality rule and are usually expressed in function of the equivalent creep strain rates $\dot{\epsilon}^{i}_{eq}$ according to :

$$\dot{\boldsymbol{\epsilon}}^{i} = \frac{3}{2}\dot{\epsilon}^{i}_{eq}\frac{\boldsymbol{s}}{\sigma_{eq}} \tag{6}$$

with σ_{eq} the Von Mises stress and $\boldsymbol{s}$ the stress deviator tensor. The equivalent creep strain rates are then defined according to the following relations:

$$\dot{\epsilon}^{irr}_{eq} = A_{irr}\sigma_{eq}\phi\exp\left(-\frac{E_{irr}}{RT}\right) \tag{7}$$

$$\dot{\epsilon}^{scat}_{eq} = A_{scat}\sigma_{eq}\frac{1}{d_g^2}\exp\left(-\frac{E_{scat}}{RT}\right) \tag{8}$$

$$\dot{\epsilon}^{disl}_{eq} = A_{disl}\sigma_{eq}^{8}d_g^2\exp\left(-\frac{E_{disl}}{RT}\right) \tag{9}$$

In Eqs. 7, 8 and 9, A_i and E_i are constant parameters, ϕ is the local fission density, d_g the grain size and σ_{eq} the Von Mises stress. The switch from scattering-creep to dislocation-creep depends on the temperature and on the stress state through the function $\theta(\sigma_{eq}, T)$. α models the increase of thermal creep with irradiation as observed for scattering-creep (Perrin, 1971). The constitutive law has been calibrated on a large database of creep compressive tests performed on non-irradiated materials (Monerie and Gatt, 2006).

3.2. Clad creep and plasticity models.

The anisotropic behavior of fresh and highly irradiated SRA Zy-4 cladding is taken into account in the fuel code Alcyone by a constitutive law coupling a creep model and a plasticity model with isotropic non-linear hardening. The formulation is based on an extensive database of creep laboratory and in-reactor tests performed at temperatures ($280 - 400$°C), stress levels ($0 - 550$ MPa), fast neutron fluxes ($1 - 2.10^{-18}$ n/m^2/s) and fluences ($0 - 10.10^{25}$ n/m^2) representative of normal and power transient conditions (Soniak et al., 2002).

As for the pellet material, the stress-strain constitutive law for the clad material is given by Hooke's law as follows :

$$\boldsymbol{\sigma} = \boldsymbol{C} : (\boldsymbol{\epsilon} - \boldsymbol{\epsilon}^{vp} - \boldsymbol{\epsilon}^{p}) \tag{10}$$

with $\boldsymbol{\epsilon}^{vp}$ the creep strain tensor and $\boldsymbol{\epsilon}^{p}$ the plastic strain tensor. The creep component of eq. 10 accounts for irradiation and thermal creep contributions and can be split as follows in rate form :

$$\dot{\boldsymbol{\epsilon}}^{vp} = \dot{\boldsymbol{\epsilon}}^{irc} + \dot{\boldsymbol{\epsilon}}^{thc} \tag{11}$$

Each of the creep components includes primary creep and secondary creep. To account for the anisotropy of the material, the creep strain rates are function of Hill's equivalent stress $\sigma_H = \sqrt{\boldsymbol{\sigma} : \boldsymbol{H} : \boldsymbol{\sigma}}$ with $\boldsymbol{H}$ a symmetric fourth rank tensor and obey the normality rule given by:

$$\dot{\boldsymbol{\epsilon}}^{i} = \dot{\epsilon}^{i}_{eq} \boldsymbol{H} : \frac{\boldsymbol{\sigma}}{\sigma_H} \tag{12}$$

with $\dot{\epsilon}^{i}_{eq}$ the equivalent creep strain rate. σ_H reads as follows when the tube reference system (r,θ,z) is used :

$$\sigma_H^2 = H_r(\sigma_{\theta\theta} - \sigma_{zz})^2 + H_\theta(\sigma_{rr} - \sigma_{zz})^2 + H_z(\sigma_{rr} - \sigma_{\theta\theta})^2 + 2H_{r\theta}\sigma_{r\theta}^2 + 2H_{rz}\sigma_{rz}^2 + 2H_{\theta z}\sigma_{\theta z}^2 \tag{13}$$

The formulation depends on three coefficients H_r, H_θ, H_z which have been identified from uniaxial and biaxial creep tests (the shear components are assumed equal to the isotropic ones, i.e., $H_{r\theta} = H_{rz} = H_{\theta z} = 1.5$). Hill's coefficients are identical for irradiation and thermal creep. The equivalent irradiation creep strain rate is expressed as follows:

$$\dot{\epsilon}^{irc}_{eq} = \dot{\epsilon}^{irc1}_{eq} + \dot{\epsilon}^{irc2}_{eq} \tag{14}$$

with the primary creep component $\dot{\epsilon}^{irc1}_{eq}$ given by :

$$\dot{\epsilon}^{irc1}_{eq} = A_{irc1} \frac{\sigma_H^{n1}}{(\epsilon^{irc1})^{n2}} \exp\left(-\frac{E_{irc1}}{RT}\right) \tag{15}$$

and the secondary creep component $\dot{\epsilon}_{eq}^{irc2}$ given by :

$$\dot{\epsilon}_{eq}^{irc2} = A_{irc2}\sigma_H^{n3}\dot{\Phi}^{n4}\exp\left(-\frac{E_{irc2}}{RT}\right) \tag{16}$$

In Eqs. (15) and (16), A_{irc1}, A_{irc2}, n_i $(i = 1, 4)$ and E_{irc1}, E_{irc2} are constant values. Creep rate enhancement due to the effect of the fast neutron flux $\dot{\Phi}$ on the material is taken into account in the stationary creep component $\dot{\epsilon}_{irc2}$. The equivalent thermal creep strain rate reads as follows:

$$\dot{\epsilon}^{thc} = V_s + \left[(V_p - V_s)\exp\left(-\frac{\epsilon^{thc}}{\epsilon_0}\right)\right] \tag{17}$$

with V_p, V_s given by :

$$V_p = V_{p0}(T, \sigma_H)V_{pf}(\Phi) \tag{18}$$

$$V_s = V_{s0}(T, \sigma_H)V_{sf}(\Phi) \tag{19}$$

and $\epsilon_0(T, \sigma_H)$ a function of temperature T and Hill's stress σ_H. V_p (primary thermal creep rate) and V_s (secondary thermal creep rate) are equal to the product of two functions which parameters are identified from tests performed on fresh Zy-4 ($V_{p0}(T, \sigma_H)$, $V_{s0}(T, \sigma_H)$) and on irradiated Zy-4 ($V_{pf}(\Phi)$, $V_{sf}(\Phi)$). The latter functions account for the reduction in thermal creep rates with irradiation, as observed experimentally (Soniak et al., 2002).

As for creep, the plastic model is based on Hill's equivalent stress with Hill's coefficients given in function of the temperature T and the fluence Φ (except the shear components). The plastic criterion is given by:

$$f(\sigma_H, \epsilon^p, T, \Phi) = f_1(\epsilon^p, T) + f_2(T, \Phi) \tag{20}$$

with $f_1(\epsilon^p, T)$ accounting for the strain-hardening of the material (ϵ^p is the equivalent plastic strain) and $f_2(T, \Phi)$ for irradiation-induced hardening. The plastic strain rate is given by the normality rule.

3.3. Pellet-clad interface friction model.

Pellet-clad friction modeling is based on Coulomb's law which relates the sliding rate v_t at the interface of two materials to the normal F_n and tangential forces F_t according to the following expression:

$$\begin{cases} v_t = 0 \quad if \quad \|F_t\| \leq \mu \|F_n\| \\ \\ v_t = -\lambda F_t \quad if \quad \|F_t\| = \mu \|F_n\| \end{cases} \tag{21}$$

where μ is the friction coefficient, λ a positive number and $\|F\|$ denotes the norm of force vector F. The Coulomb friction law is illustrated in Figure 9. Generally, a distinction is made between the coefficient of static friction when sliding is initiated $\mu = \mu_s$ and the coefficient of kinetic friction to keep sliding on-going $\mu = \mu_d$.

3.4. Material parameters for UO_2 and pellet-clad interface.

The fuel pellet crack model requires two input parameters per direction i: the fuel tensile strength f_i^t and the softening modulus K_i. A reasonable assumption is to consider the fuel tensile strength independent of the direction ($i = r, \theta, z$), i.e., $f_i^t = f_t$. Literature review shows that f_t depends greatly on temperature in the sense that a ductile-brittle transition is observed at ~ 1200°C (Canon et al., 1971, Evans and Davidge, 1969). However, for temperatures below 1200°C, the tensile strength is relatively constant and close to that measured at room temperature. Since radial cracks during ramp tests initiate at the cold pellet outer surface (temperature $<$ 500°C) and propagate at the most till the gas bubble precipitation radius where the temperature is close to the ductile-brittle transition temperature, the tensile strength used in the model is assumed independent of temperature. Based on an extensive experimental program, Radford (1979) derived analytical formulae to estimate the tensile strength at room temperature of UO_2 in function of porosity and grain size in the range 1-10% and 5-25 microns (Radford, 1979), respectively. For a standard UO_2 of porosity 3-4% and grain size 10 microns, the tensile strength is close to 130

MPa, value that is used in the simulations.

The other parameters of the fuel pellet crack model are the softening moduli K_i. It is well known that the use of material laws which account for softening leads to mesh-size dependent calculations. One way to overcome this problem is to use generalized fictitious crack models (Hillerborg et al., 1976) in which the continuum damage law is made dependent on the mesh size in order to ensure that the dissipated energy equals the fracture energy of the material. In a uniaxial tensile test such as is represented in Figure 8, the following relation holds between the fracture energy G_f, the tensile strength f_i^t, the softening modulus K_i and the mesh size in direction L_i:

$$G_f = \frac{1}{2}\frac{(f_i^t)^2}{K_i}.L_i \tag{22}$$

For UO_2, the fracture energy G_f is approximately 10 J/m^2 (Marchal et al., 2009). From Eq. 22, it stems that the softening moduli K_i are direct functions of the mesh size L_i provided the tensile strength $f_t^i = f_t = 130$ MPa and the fracture energy $G_f = 10$ J/m^2 are known. Note that these values are representative of the tensile behavior of non-irradiated UO_2 in the temperature range of interest. There might be some evolution of these quantities with irradiation, in particular when formation of the High-Burnup Structure (HBS) takes place. Since there are no experimental data available on the evolution of tensile properties of uranium oxides with irradiation, constant values are considered here in the 2D(r,θ) and 3D simulations.

Brochard and al. (2001) have summarized the test conditions and friction coefficient measures performed by different authors. Most of the tests were performed out-of-pile on non-irradiated materials and are therefore only representative of pellet-clad friction at the beginning of irradiation in commercial reactors. Different experimental set-up and conditions (pellet material, clad material, surface roughness, clad oxidation, temperature, contact pressure, sliding speed, ...) have been used by the authors. Most of the tests were performed considering a plane-plane interface between the pellet material and the cladding instead of the real fuel geometry. They found however that overall the variation range of the friction coefficient is not so

important, i.e., $0.4 < \mu < 0.69$. Among the tests, those of Nakatsuka (1981b) were performed in experimental conditions representative of a power transient, i.e., temperatures $300 - 400°C$, contact pressure 100-200 MPa (Michel et al., 2008a), internal corrosion layer of a few microns thick (Desgranges, 1998), and lead to friction coefficients in the range 0.47-0.6. In their study, Tachibana and al. (1977) showed furthermore that the static friction coefficient was only 10% higher than the kinetic friction coefficient. Since this difference falls within the dispersion of the measures, the small decrease of the friction coefficient with sliding can be neglected, i.e., $\mu = \mu_s = \mu_d$. Consistent with these results, the friction coefficient considered in Alcyone's 2D(r,θ) and 3D calculations is constant and equal to 0.5 (Sercombe et al, 2009). It is valid for non-irradiated materials only. The extension to irradiated materials is presented in the following parts.

4. Impact of friction on Pellet-Clad Interaction

4.1. Estimation of clad residual diameters

A first series of 2D(r,θ) simulations has been performed on the database of ramp tests summarized in Table 1 using the previously proposed set of parameters for the UO_2 creep, fracture and pellet-clad friction models. The creep-plasticity clad model described in Part 3.2 is applied with the material parameters that were used in the extensive validation process of the 2D and 3D schemes (Sercombe et al., 2009). In the simulation of the ramp tests, the pellet situated at the axial position of the maximum Linear Heat Rate (LHR) during ramp testing is considered. The pre-ramp state is first calculated with Alcyone by modeling the behavior of the same fuel pellet during base irradiation.

The calculated residual clad diameter increase (normalized values) during power ramp testing ($\Delta\phi_{clad}^{ramp}$) are compared in Figure 10 to the experimental measures (mean normalized values from measures performed after base irradiation and ramp test on 8 generating lines). The plain line represents the equality between calculated

and measured diameter increase. The 2D simulations lead to an average overestimation by 20% of the mid-pellet diameter increase during ramp test. These results are considered satisfactory when compared to the accuracy of the measures and the uncertainty on the ramp tests conditions. The clad deformation increase with burnup is recovered and can be attributed first, to enhanced thermal strains and fission gas-induced swelling in the pellet (Sercombe et al., 2009), second, to increased clad temperatures related to external corrosion. It is important here to stress that the simulations performed with the reference set of parameters for UO_2 lead to a reasonable estimation of clad straining and hence of pellet-clad interaction during ramp testing.

4.2. Stress distribution in the case of a viscoplastic pellet

To illustrate the impact of friction on pellet cladding interaction, the results obtained from 2D(r,θ) simulations of the power ramp performed on fuel rodlet A2 are detailed. Twenty simulations with a friction coefficient in the range $0.5 - 5$ (increasing by 0.1 up to 2 and then equal to 2.5, 3, 4 and 5) have been performed. The pre-ramp state was first calculated with Alcyone. Base irradiation of fuel rod A2 consist in two 1 year long cycles at a Linear Heat Rate (LHR) close to 200 W/cm. In the ramp test, a maximum LHR of 400 W/cm is reached and held during 12 hours. The simulations were performed assuming an infinite tensile strength to avoid cracking. Creep of the pellet is therefore the only stress-relief mechanism taken into account.

The deformed shape of the pellet fragment at the time of the maximum LHR (beginning of the holding time, point 2 in Figure 1) is illustrated in Figure 11 for a friction coefficient equal to 1.7. It is the thermal gradient in the pellet (over 1000°C) that leads to the small opening of the pellet crack (here 25 microns magnified 10 times). The opening of the crack is restricted by friction forces at the pellet clad interface which prevent significant sliding in the present calculation. In consequence of the high tangential forces that develop at the interface, a pronounced hoop stress localization in the cladding takes place in front of the crack tip, see Figure 11 (top

figure). The stress intensification factor, given by the ratio of the maximum hoop stress $= \sigma_{\theta\theta}^{max}$ to the mean hoop stress $\sigma_{\theta\theta}^{mean}$ in the cladding, is plotted in Figure 12 (with circles) in function of the friction coefficient. As expected, the maximum hoop stress increases significantly with friction (Brochard et al., 2001, Roberts, 1978). A plateau is however reached for friction coefficients greater than 2. The plateau is a consequence of the plastic behavior of the material which exhibit limited strain-hardening.

A similar spatial distribution is obtained for the plastic strains in the cladding with again a pronounced localization at the crack tip, see Figure 11 (bottom figure). Plotting in Figure 12 (with circles) the clad maximum equivalent plastic strain in function of the friction coefficient confirms in the case of a viscoplastic pellet the pronounced dependency of strain concentration on the friction forces at the pellet-clad interface.

The hoop stress distribution in the pellet at the time of maximum pellet-cladding interaction (maximum LHR, beginning of the holding period, point 2 in Figure 1) is plotted in Figure 13 for the simulation with a friction coefficient of 1.7. Owing to the thermal gradient, a rather standard distribution with compressive stresses at the pellet center and tensile stresses at the pellet periphery is obtained. Compared to that obtained in the cladding at the same time, the stress distribution is however reversed with a maximum located at the plane of symmetry of the fragment. The maximum tensile hoop stress at the pellet periphery increases by more than a factor 3 with the friction coefficient, as shown in Figure 13 (circle symbols) where all the simulation results have been reported. In the case of a friction coefficient of 0.5, representative of non-irradiated materials, the maximum hoop stress reaches already 150 MPa, which means obviously that secondary cracking during power ramps cannot be avoided (recalling that the tensile strength of the material is estimated at 130 MPa). Hoop stress saturation takes place when the friction coefficient exceeds 2 partly because of the plastic stress limitation in the cladding and partly because of creep in the pellet which increases rapidly with the stress level, see Eqs. 7-9.

Figure 14 (circle symbols) presents the evolution of the normalized residual clad diameter variation during ramp testing in function of the friction coefficient. Since stress and strain localization are enhanced by interfacial shear stresses, the residual clad diameter is significantly modified by friction in the case of a viscoplastic non brittle pellet. At the most, it increases by 15% (1 for $\mu = 0.5$, 1.15 for $\mu = 5$). Correlated with the hoop stress and inelastic strain evolution, saturation is however observed when the friction coefficient exceeds 2.

4.3. Stress distribution in the case of a brittle pellet

The same set of 2D(r,θ) simulations of ramp test A2 is proposed with this time realistic properties for the tensile strength ($f_t = 130$ MPa) and the fracture energy ($G_f = 10$ J/m^2) of uranium dioxide, see section 3.4. The hoop stress distribution in the brittle pellet is illustrated in Figure 15 for the calculation performed with a friction coefficient of 1.7 (beginning of the holding time, point 2 in Figure 1). It is obviously very different from the stress distribution obtained when creep was the only stress-relief mechanism, compare with Figure 13. While the center of the pellet is still under compression at a similar stress level, intense radial cracking of the pellet leads to a very important stress relaxation at the pellet periphery. Pellet cracking, represented in Figure 15, tends in fact to level the stresses with a maximum that never exceeds the tensile strength of the material, whatever the friction coefficient. This point is illustrated in Figure 13 by plotting the maximum tensile hoop stress in the brittle pellet as obtained from all the simulations (square symbols). The maximum hoop stress is almost constant (≈ 100 MPa) when cracking is considered in the simulations. Interestingly, since the stress level in a non-brittle pellet increases with friction, this means that the higher the friction coefficient, the greater the number of radial cracks that will develop during ramp testing. In Figure (16), the radial crack patterns obtained at the end of all the 2D(r,θ) simulations of ramp test A2 are presented. The mesh elements that appear are those where the residual strength of the material R_θ is less than 5 MPa, i.e., where local failure of

the material is achieved. As expected, the total number of radial cracks in the pellet fragment increases with friction which explains the leveling of the maximum hoop stress. Figure 16 shows that the first radial crack appears at the plane of symmetry of the fragment where the hoop stress is maximum ($\mu = 0.7$). The inward extension of this crack is important and reaches at least one third of the radius. The next radial crack divides the half fragment in two identical parts ($\mu = 1$). Its inward extension in the pellet is less pronounced than that of the first crack. Further cracking occurs with an even more reduced radial extension in the pellet.

As shown in Figure 12 (top, stress intensification factor, bottom, maximum plastic strain), pellet cracking has an important impact on stress and strain localization in the cladding (circles, calculations with the pellet creep model only, squares, calculations with the pellet creep and cracking models). Stress concentration in front of the crack tip still exist but it is limited in magnitude (maximum 1.4 compared to 2.1 when creep only is considered) and does not evolve much with friction. This is also shown by the almost constant maximum plastic strain obtained when creep and cracking of the pellet are considered. These results demonstrate the importance of radial cracking of uranium dioxide during ramp testing with respect to the risk of failure by Pellet Cladding Interaction. Since all the simulations presented here were performed with constant fracture properties, they also show the counterbalanced effect of increasing friction which tends: 1) to increase clad stresses and strains due to increasing interfacial shear forces and 2) to enhance radial cracking of the pellet which in turn leads to some leveling of the clad stresses and strains. In consequence, and opposite to the results obtained with creep only, there is no apparent variation of the normalized residual clad diameter increase during ramp test when cracking of the pellet is considered in the calculations, see the square symbols of Figure 14. Pellet-cladding friction combined to pellet cracking leads therefore to an almost stable stress and strain state in the cladding.

4.4. Friction evolution by inverse analysis.

We have shown in Part 4.3 that secondary radial pellet cracking during power ramps increases mainly with friction. The measures of radial cracks after power ramp tests show an increase of cracking with the burnup of the rodlets. Using inverse analysis the evolution of friction with burnup can therefore be deduced. Inverse analysis is based here on three components :

- experimental data, i.e., radial crack measures,
- 2D finite element simulations of the ramp tests which provide calculated estimates of radial cracking,
- one material parameter identified from the comparison of measured and calculated radial cracking, i.e., the pellet-clad friction coefficient.

The following methodology has been applied to each of the seventeen rodlets of Table 1 : sixteen 2D(r,θ) simulations of the base irradiation and power ramp are performed with friction coefficients varying between 0.5 and 2 by step of 0.1 (a total of more than 300 simulations have been performed). The number of radial cracks formed during each simulation of the power ramps is recorded (end of ramp test). The first radial crack that appears at the plane of symmetry of the fragment divides each of the 8 initial fragments in two and leads therefore to 8 new radial cracks (PR cracks). The next radial cracks that form in the bulk of the simulated half fragment divides each of the 16 initial half fragment in two and brings therefore 16 new radial cracks (PR cracks). To be consistent with the radial crack measurements, cracks in the simulations are recorded only when their radial extension exceeds 500 microns (when their extension in the radial direction is over at least 4 elements of the mesh). Applied to the crack patterns of Figure 16 (rodlet A2), this methodology leads to the evolution of the number of PR cracks with friction presented in Figure 17.

A step-wise evolution of the number of radial cracks is obtained in function of the friction coefficient. Each step characterizes the development of a new radial crack

either at the plane of symmetry of the fragment (+8) or in the bulk of the fragment (+16). Comparing these simulation results to the measured number of PR radial cracks, one can then estimate the range of friction coefficients that would lead a consistent estimate of the experimental crack pattern. For rodlet A2, Figure 17 shows that a number of measured PR radial cracks equal to 12 would be obtained in the simulations for a friction coefficient in the interval $0.7 \leq \mu \leq 0.9$. Applying the same methodology to each of the rodlets of Table 1, the evolution of the friction coefficient with the mean burnup of the rodlets has been estimated and is presented in Figure 18.
The average friction coefficient is indicated by the circles, the vertical lines give the range of friction coefficient consistent with the measured crack pattern.

The general tendency obtained from inverse analysis is of an increasing friction coefficient with the mean burnup of the rodlets. All the rodlets irradiated 2 cycles in reactor give a fairly constant friction coefficient close to 0.7-0.8, slightly higher than the one measured on non-irradiated materials (Brochard et al., 2001), i.e. 0.47-0.6. A similar distribution is obtained for the rodlets irradiated 4 cycles (mean burnup $\sim$ 50 GWd/tU) with a friction coefficient in most of the case greater than 1.5. Note that the maximum friction coefficients are close to 2 and consistent with the saturation of radial cracking obtained in the simulations for greater values, see Figure 16. For the rodlets irradiated 3 cycles (mean burnup $\sim$ 40 GWd/tU) a friction coefficient either less than 1 or greater than 1.5 has been determined by inverse analysis, depending on the duration of the holding period in the ramp test ($\mu < 1$ for holding times $<$ 15 minutes, $\mu > 1.5$ for holding times $>$ 1 h). This means that the increase of radial cracking with the holding time alone, as observed in Fig. 5 by the sharp evolution around 40 GWd/tU burnup, is not reproduced well by the simulation. A possible explanation could be an over-estimation of clad-straining (kinetics) in the first minutes of the holding period which would lead to an over-estimation of radial cracking in the simulations of the ramp tests with a short holding period. From Fig. 10, there is in fact a systematic tendency in the simulations to over-estimate clad loading during ramp testing, particularly for short

holding times. In the case of the two rodlets J3 and K3 (3 cycles, holding time < 15 minutes), the over-estimation reaches 20-30% which might therefore explain the small friction coefficients obtained by inverse analysis (0.7 and 1).

According to the simulations, radial crack evolution during the first minutes of the holding period is important. Figure (19) gives the radial crack patterns obtained at different times in the simulation of ramp test A2 (friction coefficient 1.7). It shows that if cracking is initiated during the transient period of the ramp test, there is a marked evolution of the number of radial cracks in the first 15 minutes of the holding period (24 cracks at the beginning of the holding period, 40 cracks after 15 minutes) and a stabilization after (40 cracks after 1h and 12h). An overestimation of radial crack propagation kinetics during the first minutes of the holding period could therefore also be at the origin of the lack of uniformity of the friction coefficient values obtained from the simulations of the rodlets irradiated 3 cycles.

4.5. Modeling the evolution of friction with irradiation.

From the correlation between friction and radial cracking during ramp testing, a mathematical model has been derived. It is based on the following assumptions:

- Clad-pellet friction evolves only when pellet-clad gap is closed. In normal operating conditions, pellet-clad gap closing depends on the power level reached during the first and/or the second irradiation cycle and occurs therefore for a different mean burnup depending on the rodlet irradiation history. In subsequent cycles, the pellet-clad gap remains generally closed. Suzuki et al. (2004a, 2004b) have related the evolution of pellet clad bonding to a time integral of the contact pressure at the pellet-clad interface. Proceeding in a similar manner, we propose here a relationship where the friction coefficient evolution depends on the mean burnup variation after initial pellet-clad contact. By using the mean burnup variation as the main parameter, some dependency on the contact pressure at the pellet-clad interface is introduced. The mean burnup is in fact directly correlated to the local in-reactor power level which

in turn governs the magnitude of the contact pressure.

- The evolution of friction with irradiation might depend on the formation of the HBS which initiate at an average burnup of $\sim$ 50 GWd/tU (Lemoine et al., 2010). There are naturally no direct proof of this relationship except that no re-opening of the pellet-clad gap takes place in fuel rods with a mean burnup greater than 50 GWd/tU (Desgranges, 1998). This observation is attributed to pellet-clad gap bonding and obviously a similar trend can be expected concerning friction (saturation at high burnup). This has led to the choice of an exponential function to describe friction evolution with the mean burnup variation after initial pellet-clad gap closing. A rather small evolution of the friction coefficient is thus expected between 20 and 40 GWd/tU ($\mu \approx 0.6$ at 20 GWd/tU, $\mu \approx 1$ at 40 GWd/tU) followed by a sharp increase at a higher burnup ($\mu \approx 2$ at 60 GWd/tU), see Figure 18 where an exponential relation based on a best fit of the points is represented.

- In the 2D(r,θ) simulations of the seventeen rodlets, the mean burnup at which pellet-clad gap is first closed during base irradiation (τ_0) has been systematically recorded and subtracted from the burnup at base irradiation End-Of-Life (τ_{EOL}). The following relationship between the friction coefficient μ and the variation of the mean burnup after initial pellet clad gap closing $\Delta\tau = \tau(t) - \tau_0$ (in GWd/tU) was derived by a best fit of the seventeen points relating the friction coefficient μ to $\tau_{EOL} - \tau_0$:

$$\mu = 0.56 \exp\left(0.03\Delta\tau\right) \tag{23}$$

  This relation was then used in the 2D(r,θ) simulations of the seventeen rodlets of Table 1 to check if the calculated number of PR cracks were consistent with the measured number of PR cracks. The comparison is proposed in Figure 20 where it can be seen that Eq. 23 leads overall a good approximation of the increasing number of PR radial cracks with the mean burnup of the rodlets. In particular, the experimental variation of the number of radial

cracks around $\sim$ 40 GWd/tU associated to the holding time is recovered in the simulations. It is important to recall that in the calculations performed with creep and cracking in the fuel pellet, the deformation of the cladding during base irradiation and ramp testing is not modified by friction. It means that the good agreement between calculated and measured mid-pellet clad diameter increase during ramp test illustrated in Figure 10 still holds when relation 23 is used in the simulations.

5. 3D modeling of PCI with evolving friction.

PCI is a three dimensional problem in which the behavior of pellet ends plays a crucial role with respect to the failure mechanism. To illustrate the importance of evolving friction with respect to PCI failure propensity, three dimensional simulations of rodlet G2 and M4 have been performed. Rodlet G2 was irradiated 2 cycles reaching a mean burnup of $\sim$ 25 GWd/tU and ramped at a maximum power level of 425 W/cm. Failure occurred after a few minutes. Rodlet M4 was irradiated 4 cycles reaching a mean burnup of $\sim$ 50 GWd/tU and then ramped with no failure at 460 W/cm (holding time $<$ 15 minutes). For both of the rodlets, the number of PR radial cracks were measured at mid-pellet and inter-pellet levels. At IP level, rodlet M4 has approximately twice the number of cracks of rodlet G2.

5.1. Space and time evolution of friction.

The closing of the pellet-clad gap in the 3D simulation of base irradiation of rodlet G2 is presented in Figure 21. The external pellet radii and internal clad radii at Mid-Pellet (MP) and Inter-Pellet (IP) level are plotted in function of time. Because of the hourglassing of the pellet which leads to a higher radial deformation at IP level, gap closing occurs during the first cycle at IP level and during the second cycle only at MP level. Since relation 23 depends on the burnup variation after the first pellet-clad gap closing, a marked difference in friction evolution can be

expected along the height of the pellet. The axial variation of the friction coefficient at the end of base irradiation for rodlets G2 and M4 is illustrated in Figure 22. As expected, the friction coefficient is maximum at IP level ($\mu = 1.4$ for rodlet G2 and $\mu = 2.1$ for rodlet M4) and almost constant in the remaining parts of the pellet ($\mu = 0.7$ for rodlet G2 and $\mu = 1.4$ for rodlet M4).

In consequence of this distribution, radial cracking during ramp testing is enhanced at IP level as shown by Figure 22. It is particularly true for rodlet G2 where the radial crack extension at IP level is more important than at MP level. It is less true for rodlet M4 since the friction coefficient reached a minimum value of 1.4 and led therefore to significant radial cracking everywhere along the height of the pellet. Comparing the radial crack patterns of the G2 and M4 rodlets, a significant difference can be observed owing to the higher burnup of M4 and the resulting increase of the friction coefficient. Consistent with the experimental measures after ramp tests, rodlet M4 has approximately twice the number of radial cracks of rodlet G2.

5.2. Impact of evolving friction on PCI failure propensity

The stress distribution in the cladding due to PCI depends essentially on the magnitude of radial and shear stresses at the pellet clad interface (Michel et al., 2008, Roberts, 1978). As illustrated in Figure 23 by the 3D simulation results of rodlet G2 (results given at the maximum LHR during ramp test, beginning of the holding period, point 2 in Figure 1), the axial profile of radial stress on the inner clad surface is rather discontinuous and shows a pronounced peak near the IP plane. The peak is due to the local punching induced by the hourglass deformation of the pellet during the ramp. The shear stress distribution is also characterized by a marked localization near the IP plane and in front of the fracture plane of the 3D model. Parametric 2D(r,θ) calculations of ramp tests with a radial stress and shear stress distribution similar to that obtained in Figure 23 have shown that shear stresses are by far the most important component with respect to hoop stress and strain

magnitude in front of an opening pellet crack (Michel et al., 2008a). With a mesh size of the order of the pellet crack opening (here 10-25 microns), the resulting hoop strain and hoop stress localization in the cladding can be captured in the simulations (Diard, 2001, Michel et al., 2008a). Such refinements being difficult to achieve in 3D calculations of PCI because of the complex material models and the structural non-linearities (large displacements, contact-friction), a more global failure criterion has recently been proposed from the analysis of the shear energy density at the pellet cladding interface (Michel et al., 2008). This criterion was successfully applied to compare the behavior during ramp tests of pellet materials with different tensile strength. It was shown that the reduction by a factor two of the tensile strength of UO_2 led to increasing radial cracking during power ramps and to a reduction of shear stresses at the pellet clad interface (Marchal et al., 2009, Michel et al., 2008a). In turn, the PCI failure propensity estimated from the shear energy density was strongly reduced. A basic assumption underlying the development of this purely mechanical failure criterion is the availability of a sufficient quantity of iodine to initiate stress-corrosion cracking.

In Figure 23, the radial and shear stress distributions on the inner clad surface at the maximum LHR during the ramp test (beginning of holding period, point 2 in Figure 1) of rodlet M4 are compared to those obtained for rodlet G2. Obviously the distribution of both stress components is strongly modified by the development of an important number of radial cracks in the case of rodlet M4, see Figure 22. A smoother distribution of stresses with no strong localization at the IP plane is obtained. In the case of the shear stresses, an oscillating profile in the θ direction correlated with the position of the radial cracks is obtained (with a variation of the maximum shear stress between -100 MPa and +150 MPa). Since the sliding direction is reverse on either side of each new radial crack, the shear stress changes sign. The magnitude of shear stresses is also significantly reduced by radial cracking (maximum of 205 MPa for G2 and 155 MPa for M4). A similar difference of 25% is obtained concerning the shear energy density which quantifies the gain with respect to failure risk induced by (burnup) friction-enhanced cracking in rodlet M4. In the

case of radial stresses, a smoother distribution along the pellet height with smaller maximum values is obtained for rodlet M4. This distribution is not a consequence of enhanced radial cracking but of the more important dish filling that takes place in rodlet M4 during the simulation of the ramp (at the beginning of the holding period, 3D simulations give 10% dish filling for rodlet G2 and 100% dish filling for rodlet M4). Dish filling leads to a very important radial stress relaxation mostly at the IP plane. The higher LHR in the M4 ramp test and the higher temperature in the pellet due to its higher burnup (maximum temperature 1650°C in rodlet G2, 2000°C in rodlet M4) are at the origin of the marked difference in dish filling in the simulations. Dislocation creep is the main creep mechanism during ramp testing, with a high activation energy (530 kJ/mol) which explains the marked temperature dependency.

6. Conclusions.

In this paper, 2D and 3D finite element simulations of Pellet Cladding Interaction during base irradiation and power ramps on medium to high burnup fuel rodlets have been presented. It was shown that the experimentally observed increase of pellet radial cracking during ramp test with fuel burnup could be reproduced in the simulations by the sole evolution of the pellet-clad friction coefficient with burnup. By inverse analysis based on 2D(r,θ) plane strain calculations, an exponential function relating the friction coefficient to the burnup variation after initial pellet clad contact was derived. The function was then used in 3D simulations of PCI where the differences in gap closing moments between the MP and IP planes induced by pellet hourglassing led to a marked axial variation of the pellet-clad friction coefficient. The simulated radial crack patterns were found consistent with the experimental characterization of radial cracking at MP and IP planes of medium to high-burnup fuel rodlets. An increasing number of radial cracks with the mean burnup of the rodlet was obtained both at MP and IP planes in the 3D simulations. In consequence, the shear stresses at the pellet-clad interface are strongly reduced which might explain why high burnup fuel rodlets tend to behave better in ramp tests.

As shown by the distribution of radial stresses in the 3D simulations, creep-related relaxation and dish filling might also be of importance.

The proposed approach to model friction evolution with irradiation based on the duration of the pellet-clad contact could be certainly extended to the modeling of pellet-clad bonding. The important point is to anchor the model on experimental data. While the proposed model seems adequate for ramped fuel rodlets with a medium burnup, some refinements are still necessary to catch the evolution of radial cracking during the holding period of the power ramp in the case of high burnup fuel rods. This paper gives however a good illustration of how radial cracking can be included in the validation process of a fuel code.

Acknowledgement

The authors would like to thank EDF and AREVA for their financial and technical support to this research.

List of Tables

Table 1: Main ramp test parameters of the database.

Rodlet	Burnup (GWd/tU)	Max. power (W/cm)	Holding time
A2	~ 25	400	12 h
B2	~ 25	450	< 15 min
C2	~ 25	460	< 15 min
D2	~ 25	470	2 h
E2	~ 25	530	< 15 min
F2	~ 25	410	< 15 min
G2	~ 25	425	< 15 min
H3	~ 40	430	12 h
I3	~ 40	400	2 h
J3	~ 40	530	< 15 min
K3	~ 40	520	< 15 min
L4	~ 50	430	4 h
M4	~ 50	460	< 15 min
N4	~ 50	440	1 h
O4	~ 50	430	12 h
P4	~ 50	440	6 h
Q4	~ 60	410	12 h

Table 2: Summary of the models used in the fuel thermo-mechanical code Alcyone.

Fuel properties	
Thermal conductivity	Modified Lucuta's formulation (Lucuta et al., 1996)
Thermal expansion coefficient	Martin's formulation for UO_2 (Martin, 1988)
Elasticity coefficients	Martin's formulation for temperature dependency (Martin, 1989)
Creep	Irradiation, scattering and dislocation creep (Monerie and Gatt, 1996)
Cracking	(r, θ, z) smeared crack model (Michel et al., 2008b)
Densification - solid swelling	(MATPRO, 1997)
Radial power profiles	Modified version of RADAR (Palmer, 1992)
Gaseous swelling	stress-dependent intra- and inter-granular bubble swelling model (Garcia, 1998)
Clad properties	
Thermal conductivity	SRA Zy-4 temperature-dependent model (MATPRO, 1997)
Thermal expansion coefficient	SRA Zy-4 anisotropic model (Internal CEA report, 1981)
Elasticity coefficients	SRA Zy-4 isotropic model (Internal CEA report, 1981)
Inelastic clad behavior	SRA Zy-4 anisotropic formulation based on Hill's criterion (Soniak, 2002) Irradiation-induced creep, low-stress creep High-stress creep and plasticity
Pellet-clad interface	
Pellet-clad gap thermal heat transfer	URGAP model (Lassmann and Hohlefeld, 1987)
Friction between pellet and cladding	Coulomb law (Cast3M, 2011)

List of Figures

Figure 13: Hoop stress distribution for a friction coefficient of 1.7 (top) and maximum hoop stress in the pellet versus friction coefficient (bottom) in the 2D(r,θ) simulations of A2 ramp test.

Figure 14 : 2D(r,θ) calculated mid-pellet diameter increase during ramp testing (normalized values) versus friction coefficient.

Figure 15 : Hoop stress and radial crack distribution in the pellet in the 2D(r,θ) simulations of A2 ramp test (friction coefficient 1.7).

Figure 16 : Calculated radial cracking after ramp test A2 versus friction coefficient.

Figure 17 : Calculated number of PR radial cracks after ramp test A2 versus friction coefficient.

Figure 18 : Evolution of the friction coefficient with the mean burnup of the rodlet as estimated from 2D(r,θ) simulations.

Figure 19 : Calculated evolution of radial pellet cracking during ramp test A2 (friction coefficient 1.7).

Figure 20 : Calculated and measured number of PR cracks in function of the mean burnup of the rodlets.

Figure 21 : Evolution in the 3D simulations of the pellet clad-gap at Mid-Pellet and Inter-Pellet level during base irradiation of rodlet G2.

Figure 22 : Calculated distribution of radial cracks (left) and friction coefficient (right) at the end of the 3D simulations of ramp tests G2 (top) and M4 (bottom).

Figure 23 : Distribution of radial stresses (left) and shear stresses (right) on the pellet-clad interface at the time of the maximum LHR during the 3D simulations of ramp tests G2 (top) and M4 (bottom).

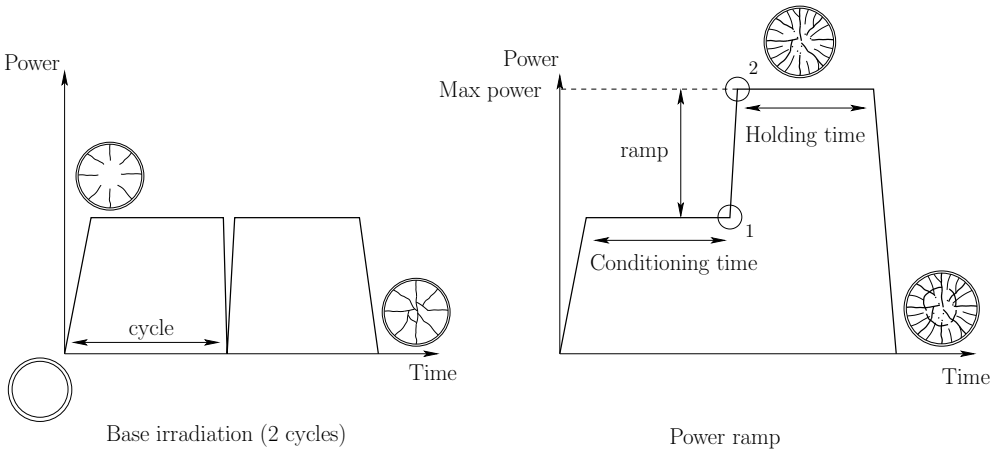

Figure 1: Irradiation history and pellet radial crack pattern during normal (base irradiation) and off-normal (power ramps) operating conditions.

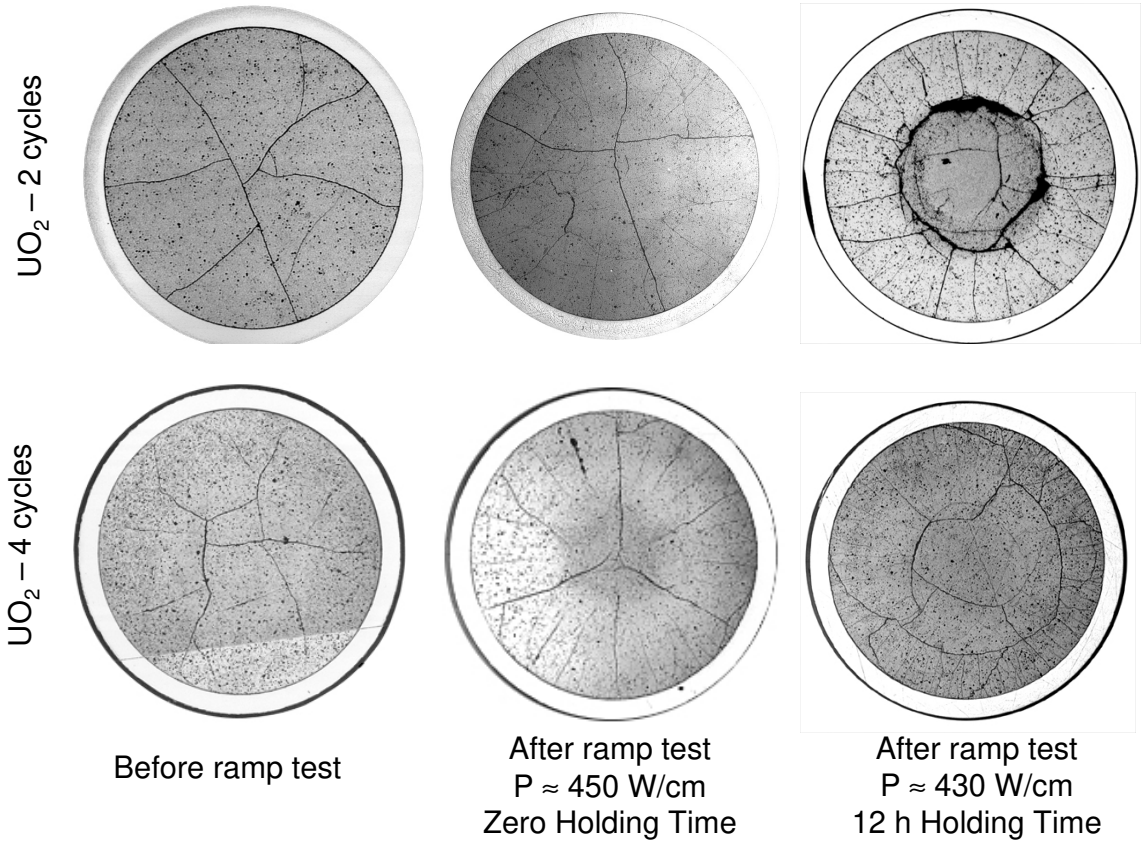

Figure 2: Cross-sections of UO_2 fuel rodlets (mean burnup ~ 25 and ~ 50 GWd/tU) after 2 and 4 cycles irradiation in a PWR commercial reactor (left), after zero holding time power ramps (middle) and after 12h long power ramps (right).

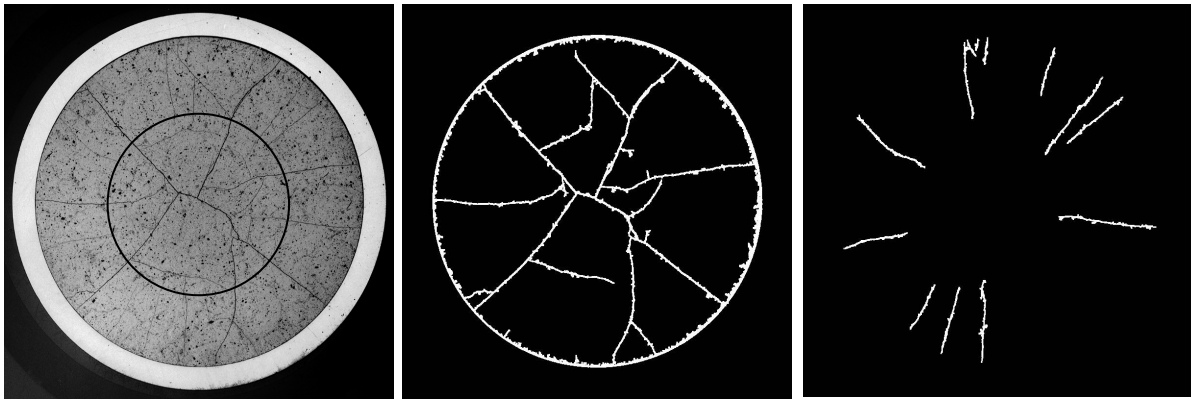

Ceramography | Base Irradiation cracks (8) | Power ramp cracks (11)

Figure 3: Illustration of radial crack counting from the Mid-Pellet cross-section of fuel rodlet F2.

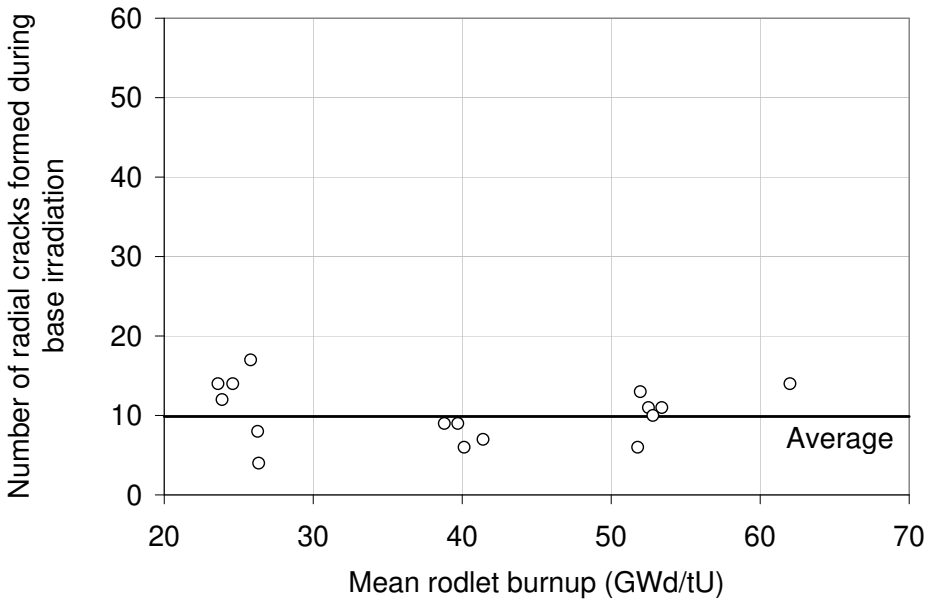

Figure 4: Evolution of radial pellet cracking at the end of base irradiation with the mean burnup of the rodlet.

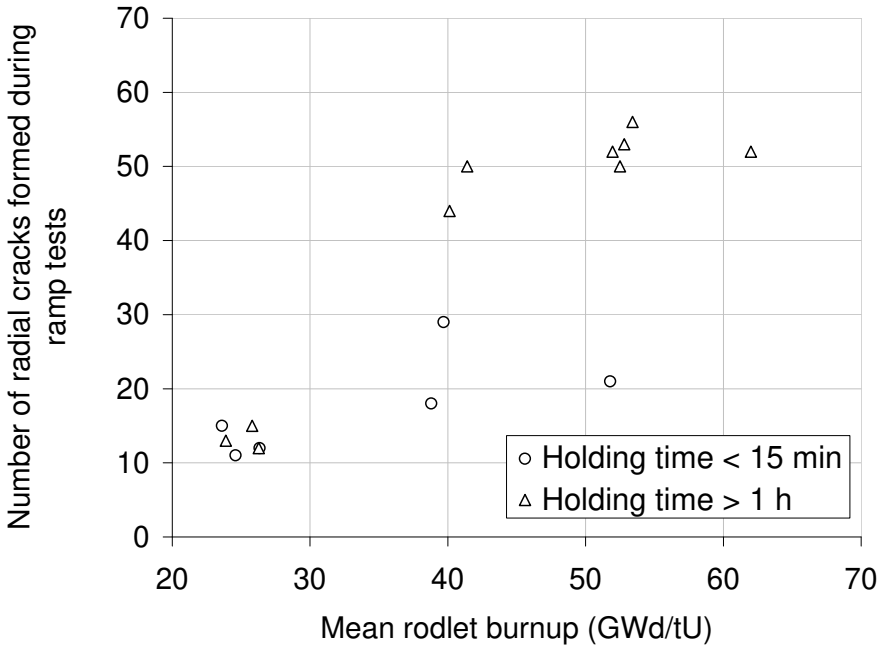

Figure 5: Evolution of radial pellet cracking at the end of ramp test with the mean burnup of the rodlet.

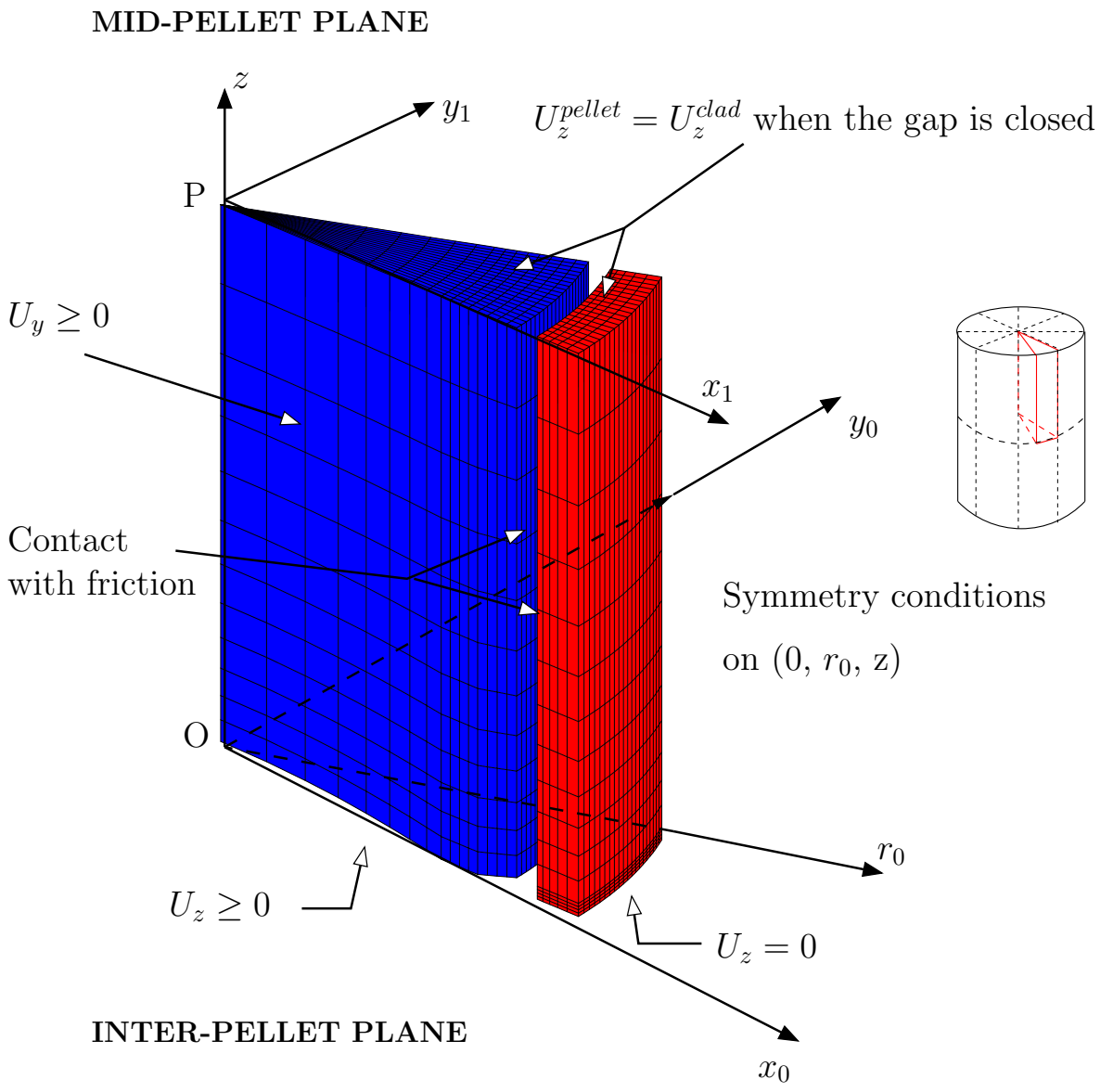

Figure 6: Mesh and boundary conditions in Alcyone 3D simulations.

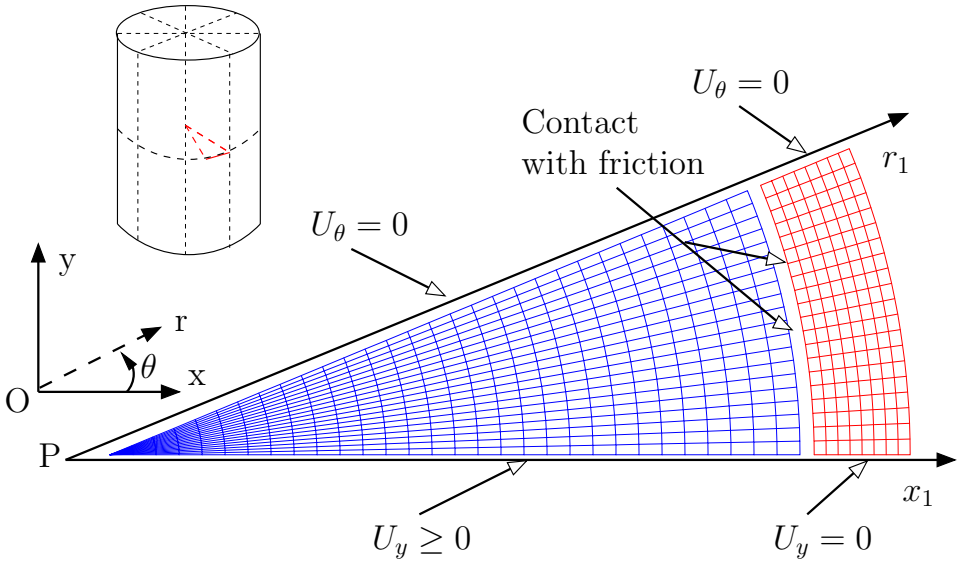

Figure 7: Mesh and boundary conditions in Alcyone 2D(r,θ) simulations.

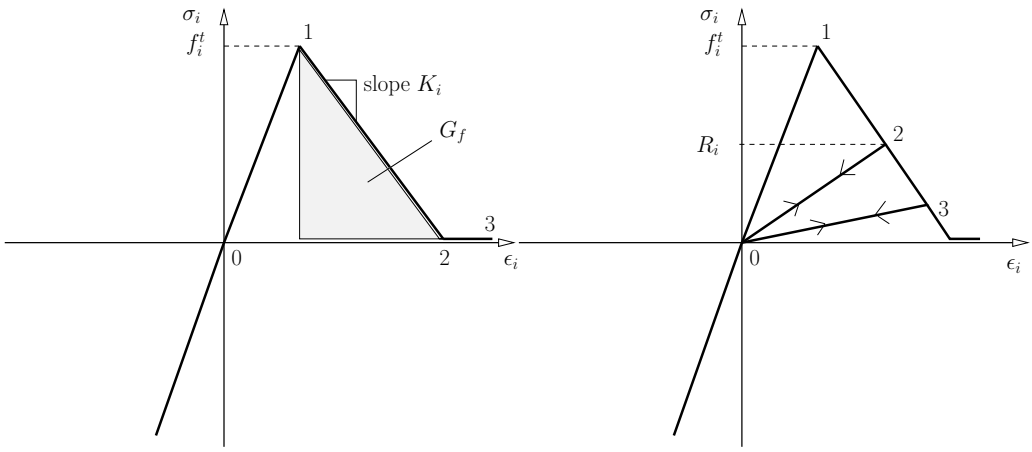

Figure 8: Stress-strain relation during monotonic (left) and cyclic (right) tensile loading.

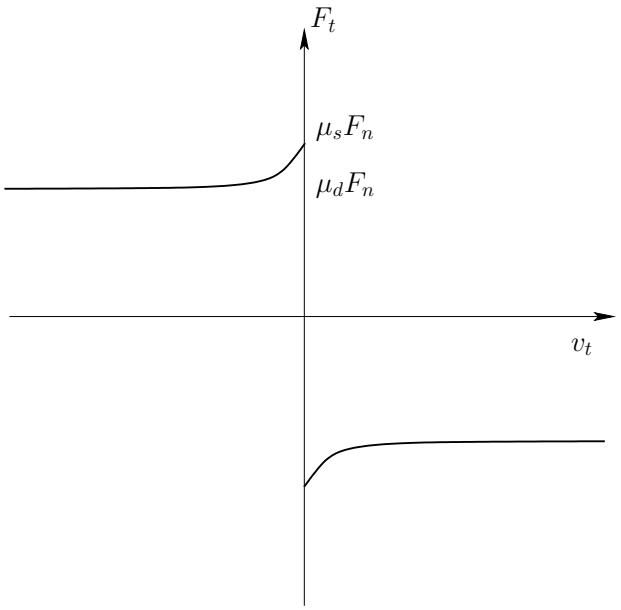

Figure 9: Pellet clad friction model of Alcyone

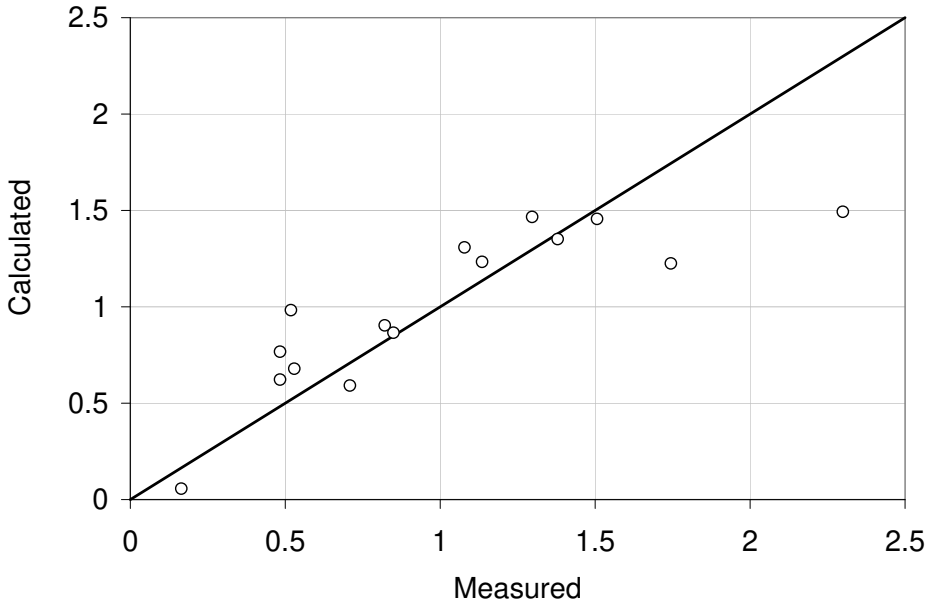

Figure 10: 2D(r,θ) calculated and measured mid-pellet diameter increase during ramp testing (normalized values).

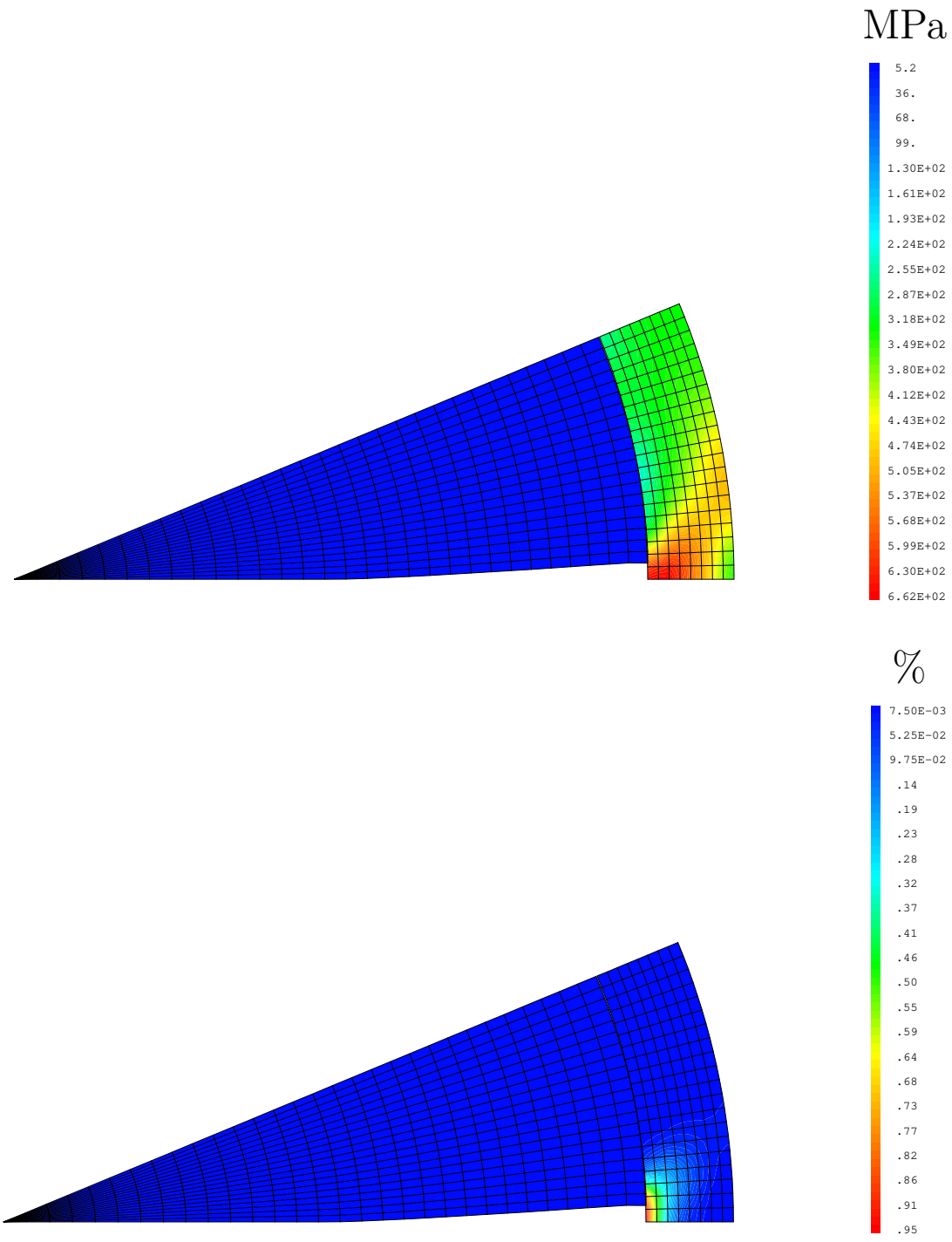

Figure 11: Hoop stress (top) and equivalent plastic strain (bottom) distributions in the cladding at the maximum LHR of A2 ramp test (friction coefficient 1.7).

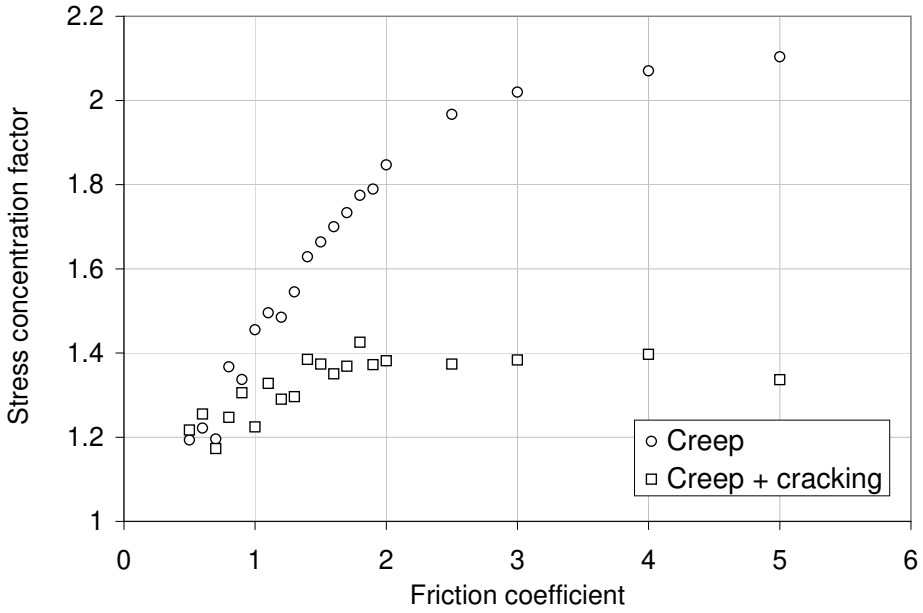

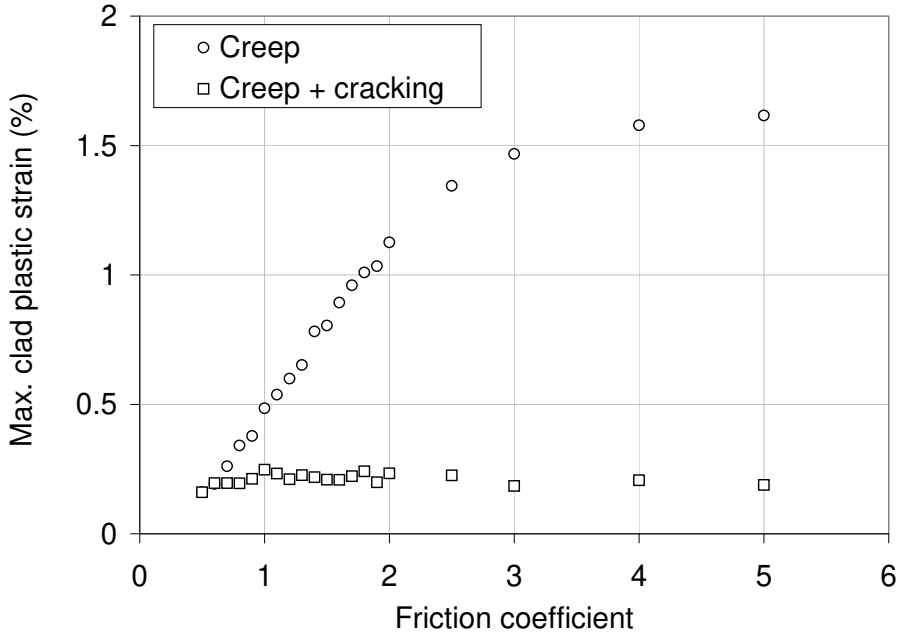

Figure 12: Maximum hoop stress intensification factor and maximum equivalent plastic strain in the cladding versus friction coefficient in the 2D(r,θ) simulations of A2 ramp test.

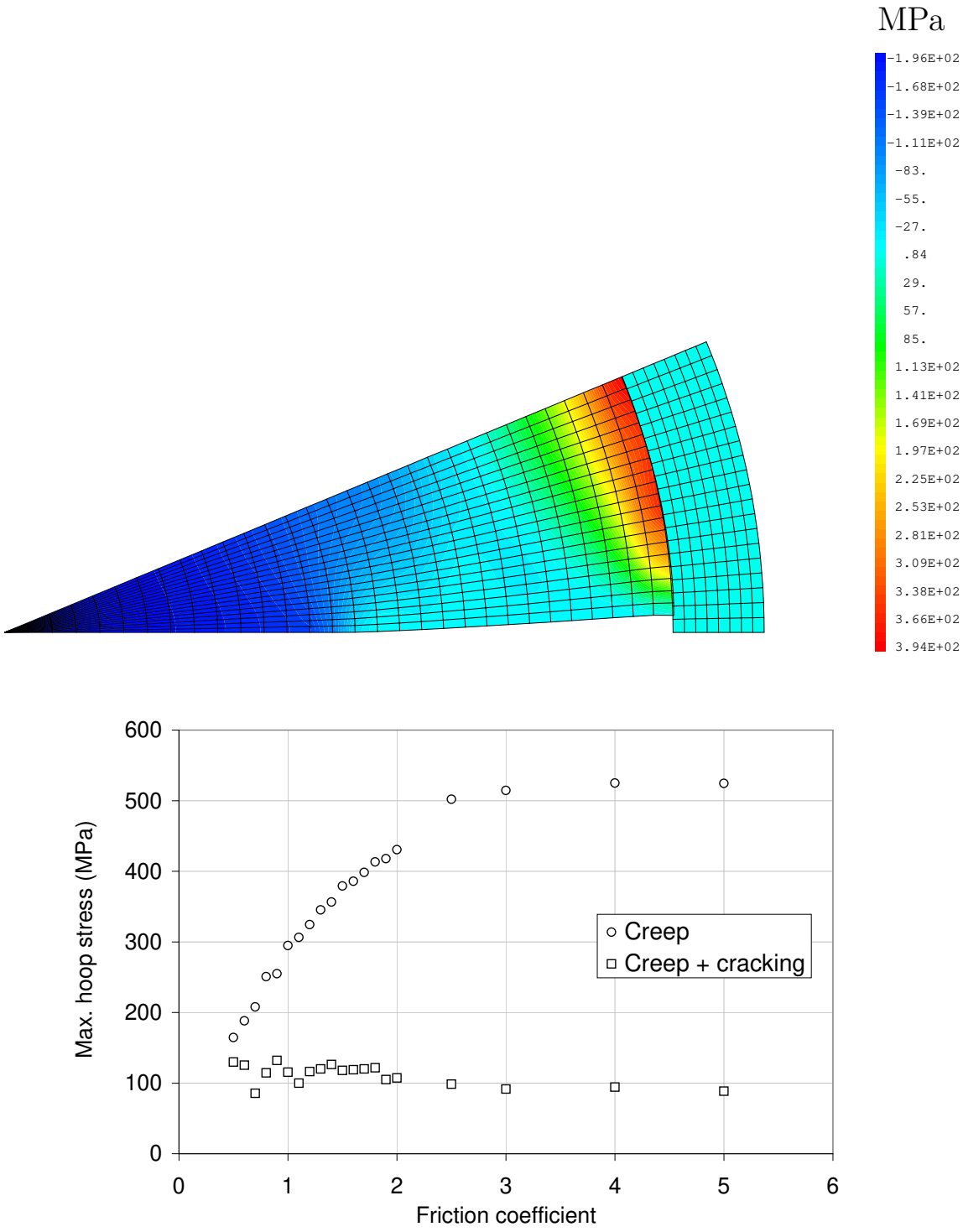

Figure 13: Hoop stress distribution for a friction coefficient of 1.7 (top) and maximum hoop stress in the pellet versus friction coefficient (bottom) in the 2D(r,θ) simulations of A2 ramp test.

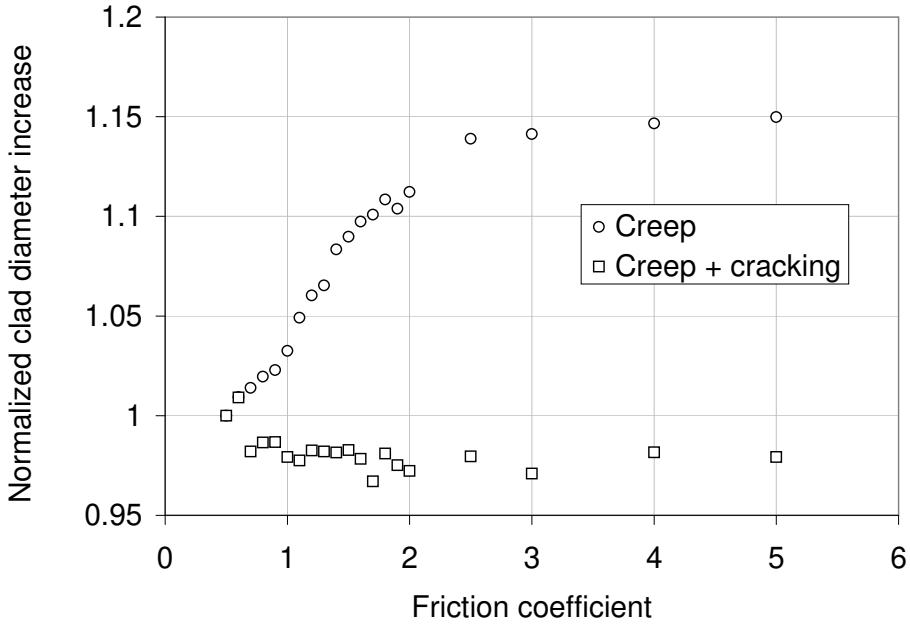

Figure 14: 2D(r,θ) calculated mid-pellet diameter increase during ramp testing (normalized values) versus friction coefficient.

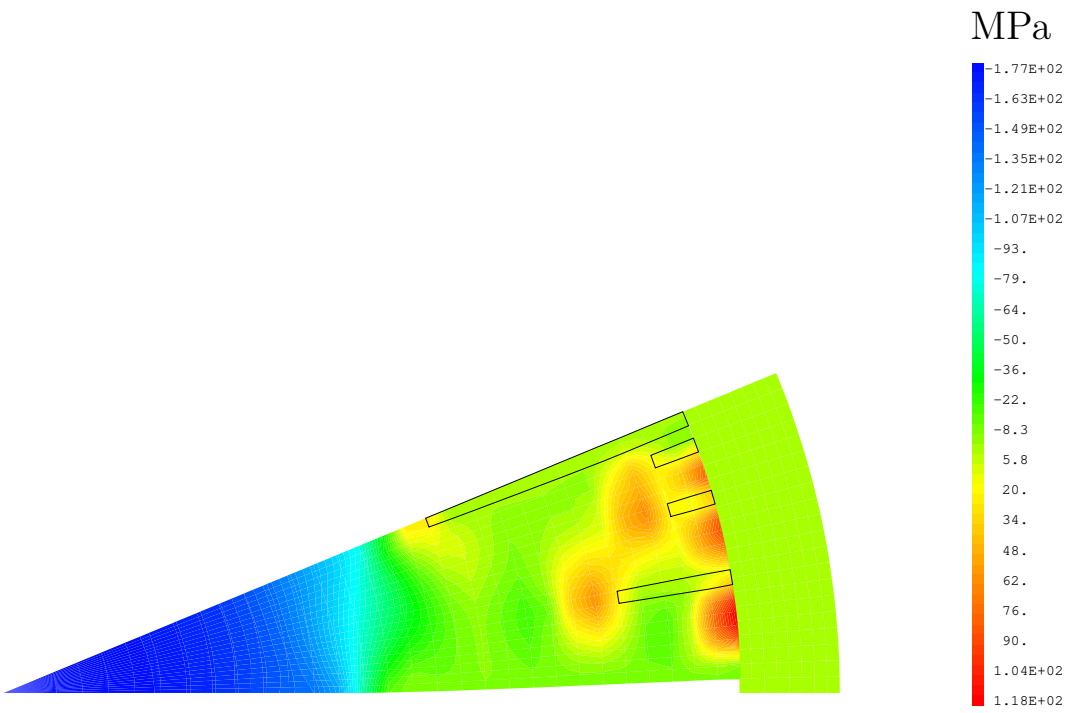

Figure 15: Hoop stress and radial crack distribution in the pellet in the 2D(r,θ) simulations of A2 ramp test (friction coefficient 1.7).

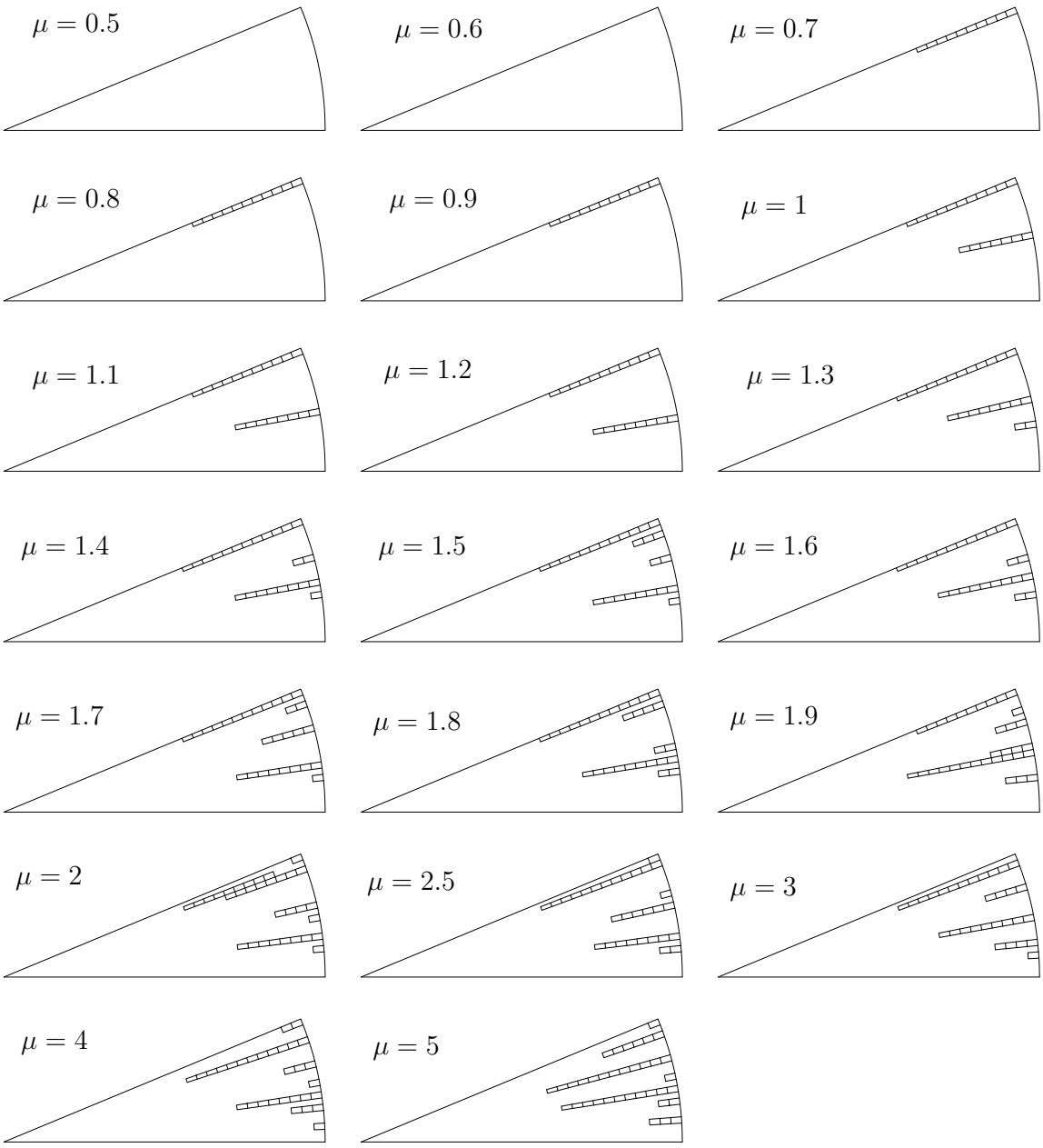

Figure 16: Calculated radial cracking after ramp test A2 versus friction coefficient.

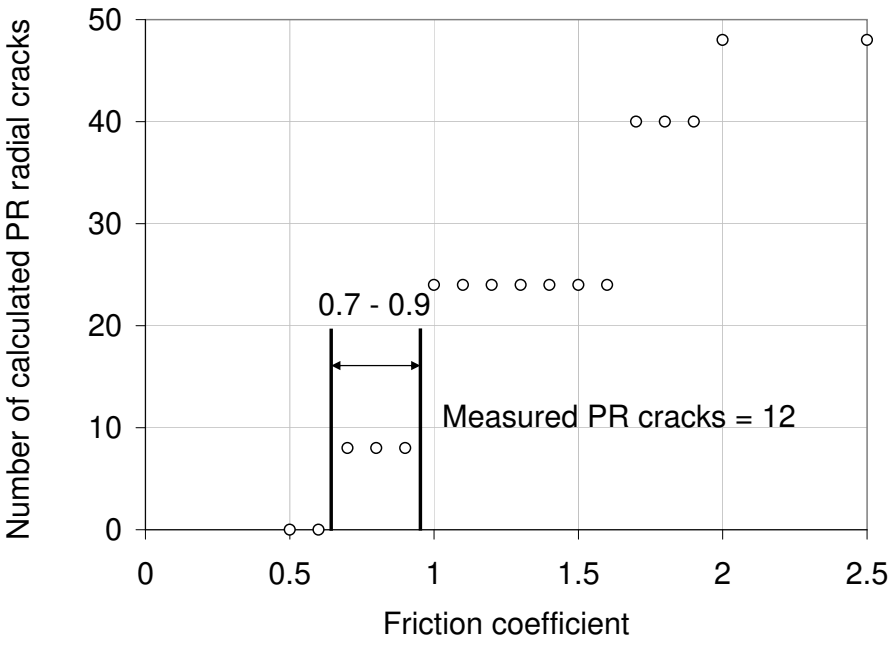

Figure 17: Calculated number of PR radial cracks after ramp test A2 versus friction coefficient.

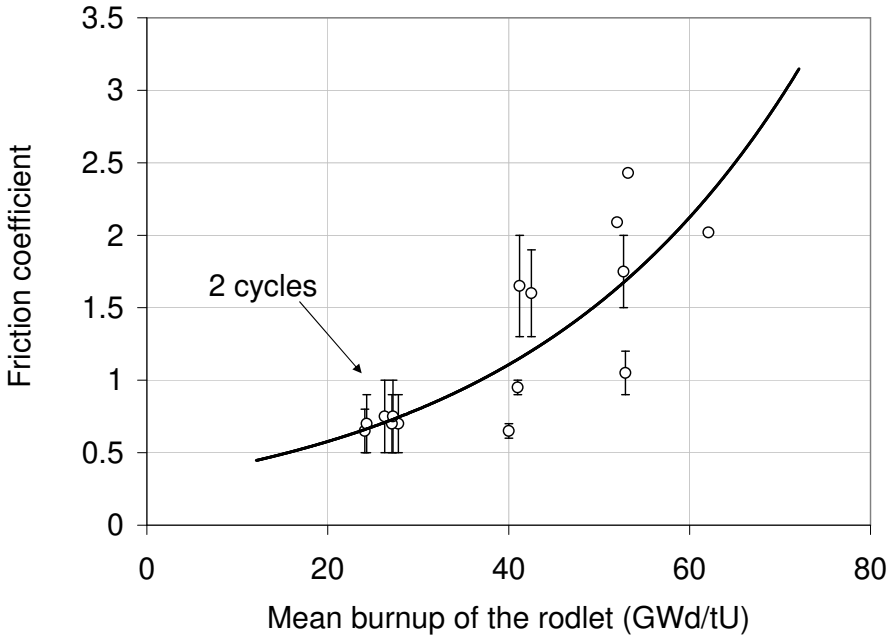

Figure 18: Evolution of the friction coefficient with the mean burnup of the rodlet as estimated from 2D(r,θ) simulations.

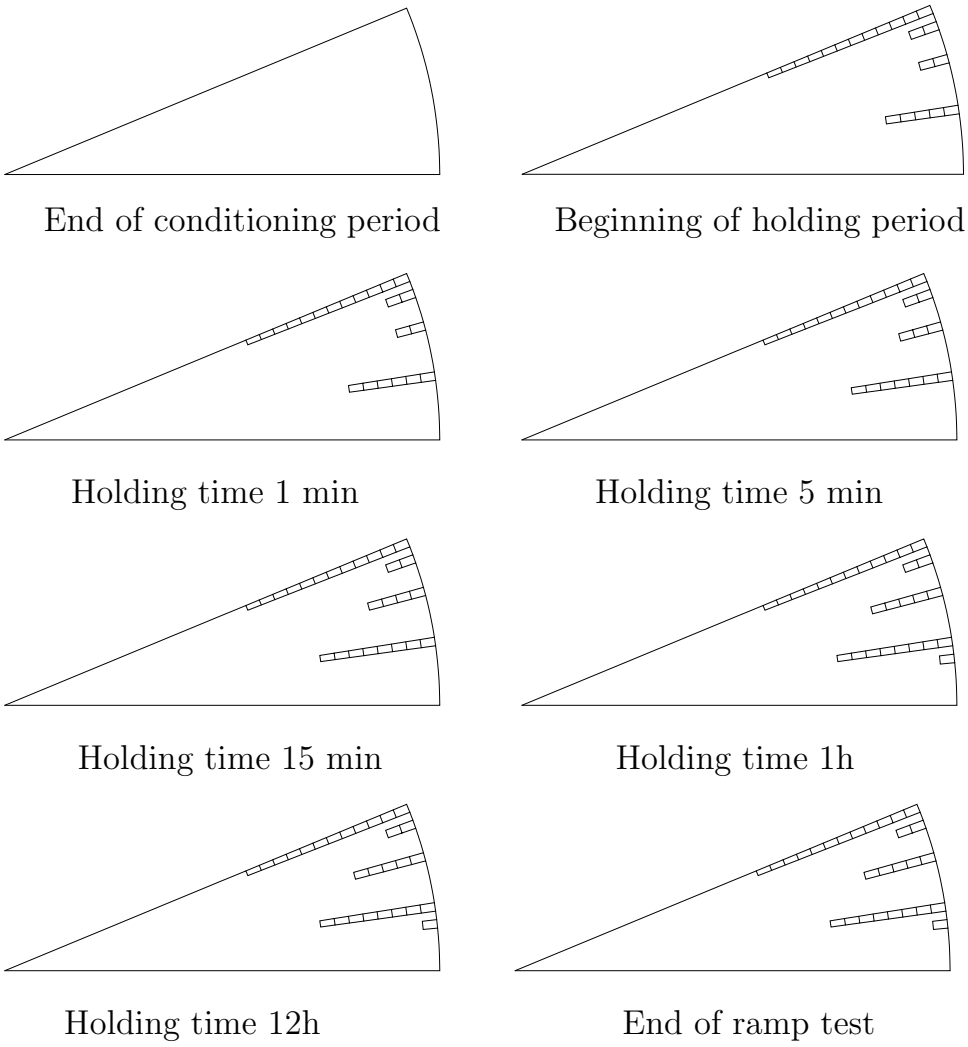

Figure 19: Calculated evolution of radial pellet cracking during ramp test A2 (friction coefficient 1.7).

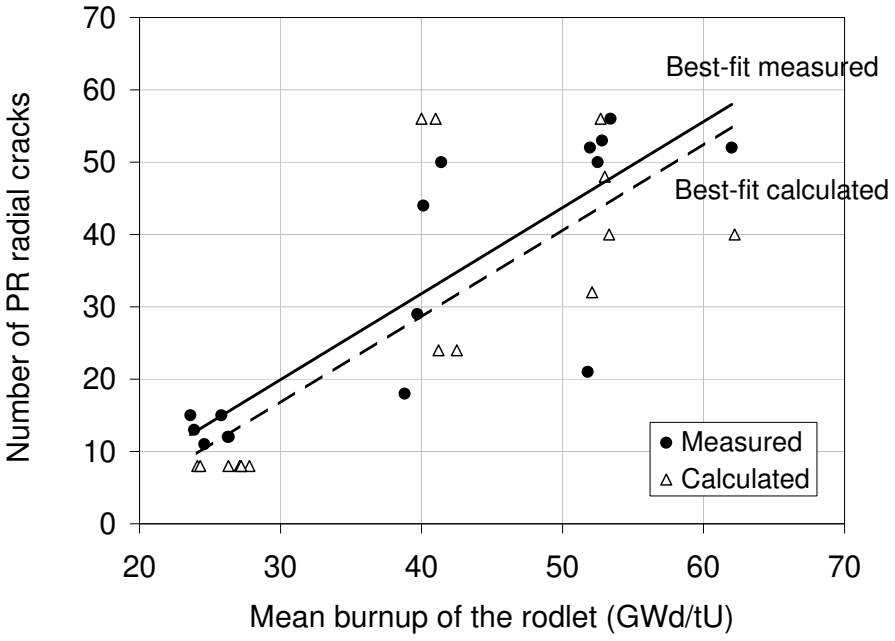

Figure 20: Calculated and measured number of PR cracks in function of the mean burnup of the rodlets.

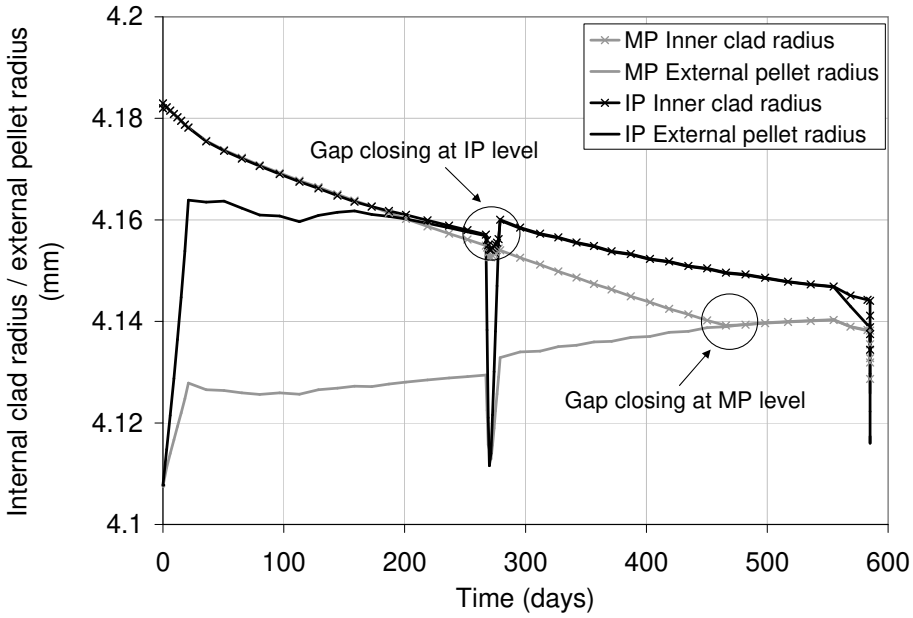

Figure 21: Evolution in the 3D simulations of the pellet-clad gap at Mid-Pellet and Inter-Pellet level during base irradiation of rodlet G2.

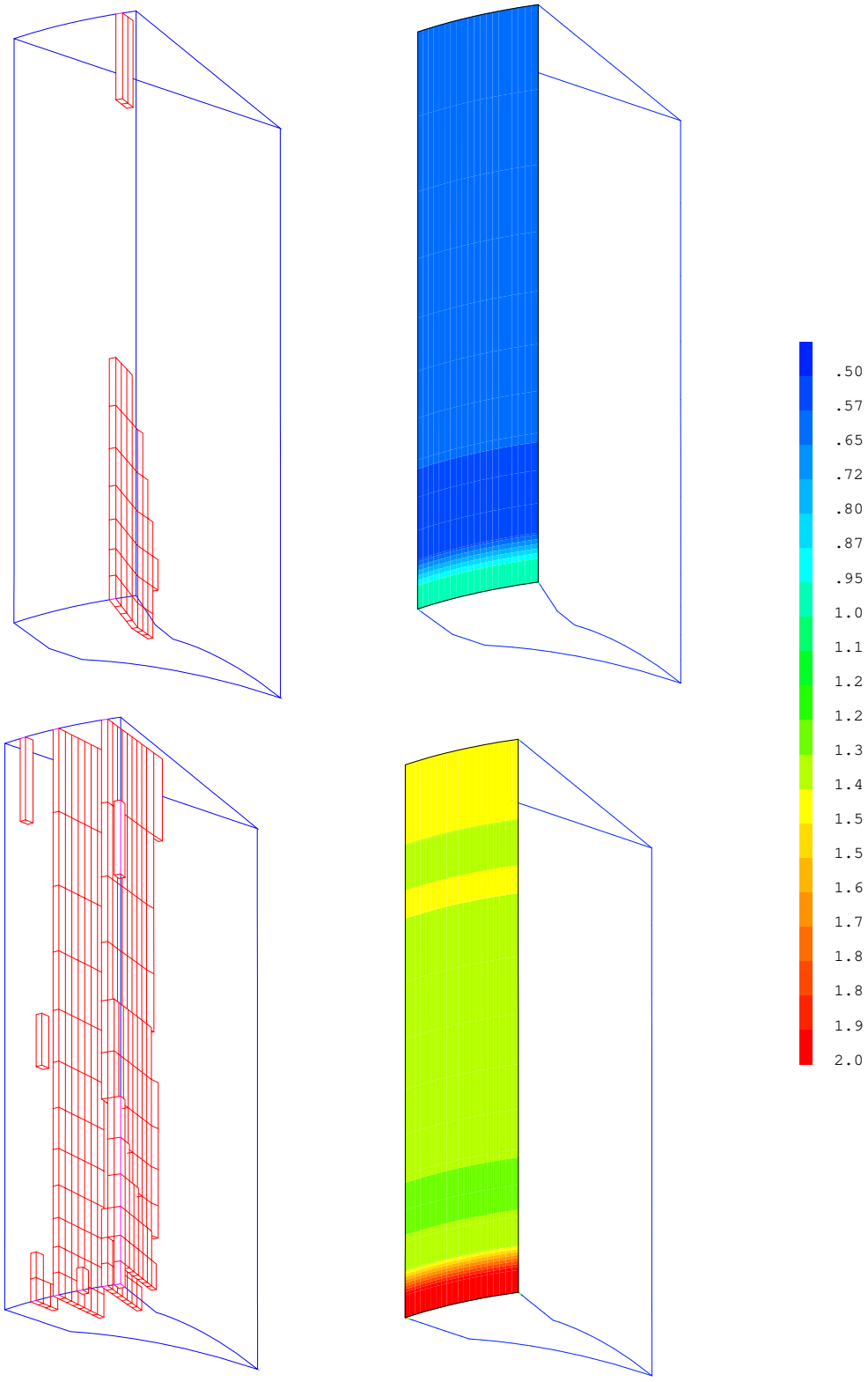

Figure 22: Calculated distribution of radial cracks (left) and friction coefficient (right) at the end of the 3D simulations of ramp tests G2 (top) and M4 (bottom).

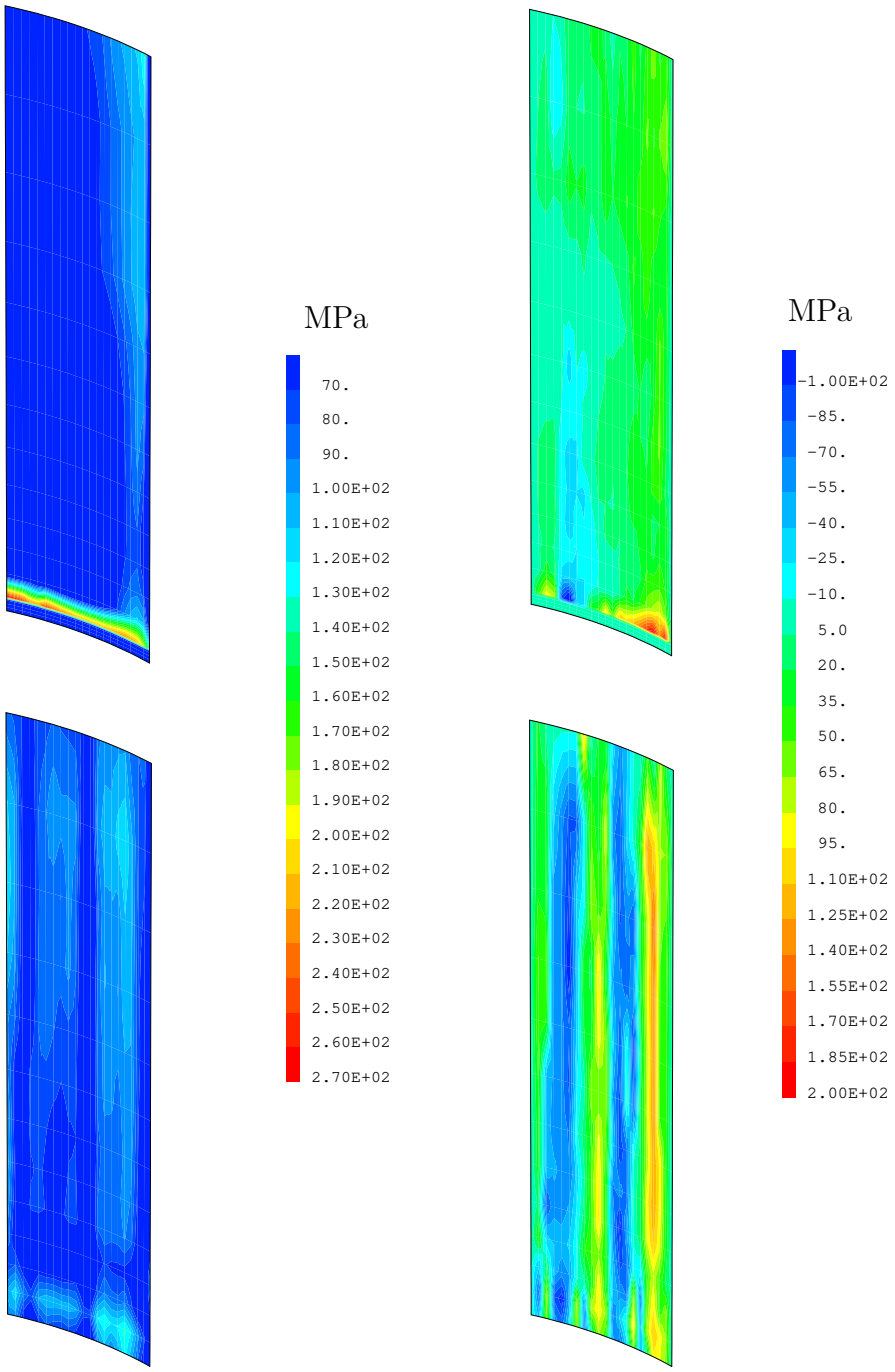

Figure 23: Distribution of radial stresses (left) and shear stresses (right) on the pellet-clad interface at the time of the maximum LHR during the 3D simulations of ramp tests G2 (top) and M4 (bottom).